

A 3D unstructured grid nearshore hydrodynamic model based on the vortex force formalism



Peng Zheng^{a,*}, Ming Li^a, Dominic A. van der A^b, Joep van der Zanden^{b,c}, Judith Wolf^d, Xueen Chen^e, Caixia Wang^f

^a School of Engineering, University of Liverpool, Liverpool, England L69 3GQ, United Kingdom

^b School of Engineering, University of Aberdeen, Aberdeen AB24 3 UE, United Kingdom

^c Department of Water Engineering and Management, University of Twente, PO Box 217, Enschede 7500 AE, The Netherlands

^d National Oceanography Centre, Joseph Proudman Building, 6 Brownlow Street, Liverpool, England L3 5DA, United Kingdom

^e School of Physical and Environmental Oceanography, Ocean University of China, Qingdao 266100, China

^f Tianjin Binhai New Area Bureau of Meteorology, 26 Taixiang Road, Binhai New Area, Tianjin 300457, China

ARTICLE INFO

Article history:

Received 28 November 2016

Revised 1 June 2017

Accepted 10 June 2017

Available online 13 June 2017

Keywords:

Unstructured grid

Vortex-force

Wave-current interaction

FVCOM

Unstructured SWAN

ABSTRACT

A new three-dimensional nearshore hydrodynamic model system is developed based on the unstructured-grid version of the third generation spectral wave model SWAN (Un-SWAN) coupled with the three-dimensional ocean circulation model FVCOM to enable the full representation of the wave-current interaction in the nearshore region. A new wave-current coupling scheme is developed by adopting the vortex-force (VF) scheme to represent the wave-current interaction. The GLS turbulence model is also modified to better reproduce wave-breaking enhanced turbulence, together with a roller transport model to account for the effect of surface wave roller. This new model system is validated first against a theoretical case of obliquely incident waves on a planar beach, and then applied to three test cases: a laboratory scale experiment of normal waves on a beach with a fixed breaker bar, a field experiment of oblique incident waves on a natural, sandy barred beach (Duck'94 experiment), and a laboratory study of normal-incident waves propagating around a shore-parallel breakwater. Overall, the model predictions agree well with the available measurements in these tests, illustrating the robustness and efficiency of the present model for very different spatial scales and hydrodynamic conditions. Sensitivity tests indicate the importance of roller effects and wave energy dissipation on the mean flow (undertow) profile over the depth. These tests further suggest to adopt a spatially varying value for roller effects across the beach. In addition, the parameter values in the GLS turbulence model should be spatially inhomogeneous, which leads to better prediction of the turbulent kinetic energy and an improved prediction of the undertow velocity profile.

© 2017 The Authors. Published by Elsevier Ltd.

This is an open access article under the CC BY license. (<http://creativecommons.org/licenses/by/4.0/>)

1. Introduction

The interaction of wind-generated surface gravity waves with slowly varying ocean currents in shallow coastal areas can create unique flow patterns (e.g. longshore current, rip current and undertow) in both inner shelf and surf zone environments. The investigation of wave-current interaction under propagating surface waves is especially important to coastal engineers and provides the basis for morphodynamic modeling. The main effects of cur-

rents on the waves are the current-induced refraction and Doppler frequency shift (Kumar et al., 2012; hereafter K12). The wave effects on current (hereinafter WEC) are more complicated and diverse, ranging from wave-induced upper-ocean mixing and current profiles to littoral flow, sea level set-up/set-down and near bed streaming. These effects often play important role in determining local sediment transport and hence the overall morphological evolution (Van Rijn et al., 2013).

Since the fundamental work of Longuet-Higgins and Stewart (1964) in the last century, a large number of theoretical approaches and implementations have been proposed for coupling the surface wind waves with ocean circulation (Bowen et al., 1968; Haselmann, 1971; Craik and Leibovich, 1976; Garrett, 1976; Phillips, 1977). Most of these early studies investigated the interplay

* Corresponding author.

E-mail addresses: zp112@liverpool.ac.uk, hotspring112@gmail.com (P. Zheng), m.li@liverpool.ac.uk (M. Li), d.a.vandera@abdn.ac.uk (D.A. van der A), j.vanderzanden@utwente.nl (J. van der Zanden), jaw@noc.liv.ac.uk (J. Wolf), xchen@ouc.edu.cn (X. Chen), cwang1988@163.com (C. Wang).

<http://dx.doi.org/10.1016/j.ocemod.2017.06.003>

1463-5003/© 2017 The Authors. Published by Elsevier Ltd. This is an open access article under the CC BY license. (<http://creativecommons.org/licenses/by/4.0/>)

between waves and currents in forms that the additional wave forcing for the total momentum (i.e. including waves and currents), derived as a net wave-induced momentum flux, is represented as the divergence of radiation stress tensor (Longuet-Higgins and Stewart, 1964; Smith 2006; and Mellor 2003, 2005, 2011, G. 2015). Unfortunately, the vertical flux requires an approximation to first order in the wave-induced pressure and velocities, which is often difficult to resolve (Ardhuin et al., 2008b; Bennis et al., 2011). Hence, most applications have rather used the conceptually more difficult equations for the current momentum only. These are usually cast in a form that involves a vortex force (VF, Craik and Leibovich, 1976; McWilliams et al., 2004; Ardhuin et al., 2008a; Aiki and Greatbatch, 2013), though they can also be equivalently written with a different form (Suzuki and Fox-Kemper, 2016).

In recent years, the VF formalism has been widely used to represent the additional terms corresponding to WEC in the momentum equations. It splits the wave-averaged effects into gradients of Bernoulli head and a vortex force and has a primary advantage of explicitly including a type of wave–current interaction that few if any available wave models properly incorporate to allow its complete expression in the radiation stress (Uchiyama et al., 2010, hereinafter U10; Newberger and Allen 2007a, 2007b, hereafter NA07; McWilliams et al. 2004, hereinafter MRL04). As a result, the VF method is able to explicitly separate the different contributions in pressure distribution which is particularly important to verify the model's characteristics through the momentum balance as demonstrated by U10. However, most of the existing studies using VF methods are limited to structured grid models. In practical engineering applications, the unstructured grid model has distinct advantages in dealing with complicated domain and local refinement around rapidly varying bathymetry, for instance around structures, that are not easily achievable in a structured grid (Wang and Shen, 2011). With the potential of dynamic mesh adaptation using an unstructured grid, the model is also able to deal with simulations involving strong spatial and temporal variations, as shown in Huang et al. (2008).

In addition, the proper description of the turbulence characteristics is also often crucial for the simulation of WEC due to wave breaking as demonstrated by many existing studies. However, most of the former studies are based on models such as $k-\varepsilon$, $k-kl$ that are calibrated for an equilibrium turbulence production and dissipation state, which are strictly speaking not applicable for the simulation of the wave breaking process (Burchard, 2001; Umlauf and Burchard, 2003). The K-profile parameterization (KPP) is also found difficult to represent accurately the mixing in the bottom boundary layer and in nearshore regions (Durski et al., 2004). Partly, this is due to the fact that to develop and verify a turbulence scheme's suitability in modeling wave breaking, much detailed measurements in laboratory controlled conditions in both flow hydrodynamics and turbulence characteristics, as well as free surface variations are required. But such comprehensive datasets are still scarce in the literature. With few most recent experimental studies, e.g. van der A et al. (2017) and van der Zanden et al. (2016), it is possible to implement practical turbulence closure coupling with the WEC processes for better model accuracy in simulating wave breaking and wave–current interactions.

The above considerations motivated the development of a new three-dimensional coastal hydrodynamic model system with fully coupled 3D wave–current interactions on an unstructured grid, which can be used as a basis for an effective morphodynamic model system. This is achieved by coupling the unstructured version of the third generation wind wave model, Simulating WAVes Nearshore (hereinafter Un-SWAN, Booij et al., 1999; Zijlema, 2010), as wave module to the unstructured-grid, three-dimensional oceanic circulation model, Finite Volume Coastal Ocean Model (FVCOM, Chen et al., 2003). A new wave–current interaction scheme

based on a VF approach (MRL04, U10) is implemented into FVCOM to account for wave effects on currents (WEC). The Generic Length Scale (GLS; Umlauf and Burchard, 2003) scheme is incorporated and modified to better account for the wave-enhanced turbulence generation, dissipation and vertical mixing in breaking-wave conditions. A wave roller transport model is implemented in this modeling system to account for wave breaking under influence of the surface wave roller, which is absent in original FVCOM code. In addition, a new coupling module is also developed to facilitate the communication between Un-SWAN and FVCOM, and realize the model coupling procedure. It should be noted that the present study differs fundamentally from the previous FVCOM-SWAVE work of Qi et al. (2009) and subsequently Wu et al. (2011) and Sun et al. (2013) in many aspects, e.g. the WEC is represented through VF approach and the original unstructured SWAN is employed with a new coupling method.

The outline of this paper is as follows. Section 2 fully presents the modeling system, while its numerical implementation is described in Section 3. The model system is firstly validated with a theoretical case of obliquely incident waves on a planar beach in Section 4. Section 5 presents the validation of the model against three additional cases: (a) a large-scale laboratory experiment involving normal incident wave breaks over a naturally formed breaker bar; (b) a real field experiment of obliquely incident waves on a natural, sandy, barred beach (Duck' 94 experiment); and (c) a laboratory scale experiment of normally incident waves on plane beach with a shore-parallel breakwater. Finally, the summary and conclusions are given in Section 6.

2. The numerical model

The present model system is based on the Finite Volume Coastal Ocean Model (Chen et al., 2003) and the unstructured version of the third generation wind wave model SWAN (Booij et al., 1999; Zijlema, 2010). The original FVCOM has no direct coupling measures with Un-SWAN. In this study, the Un-SWAN is therefore adapted and merged into FVCOM and a new specific coupler module is developed for the two-way dynamic coupling between the circulation model and wave model. In addition, the GLS based turbulence model is implemented together with the current model to resolve wave breaking and turbulence dissipation properly. All of these modules are developed to be consistent with the framework of FVCOM.

2.1. Wave model

In this study, the widely-used third generation SWAN (Booij et al., 1999) spectral wave model is adapted to provide the necessary forcing terms for the coastal circulation model. For given wind, bathymetry and current conditions, SWAN provides the spectral and integral wave properties of random short-crested wind-generated waves by solving a spectral action balance equation that includes wave energy dissipation due to bottom friction, triad and quadruplet wave–wave interactions and shallow water wave-breaking, without any *a priori* restrictions on the spectrum for the evolution of wave growth. The wave action balance equation is represented as

$$\frac{\partial N(\sigma, \theta; x, y, t)}{\partial t} + \frac{\partial c_{g,x} N(\sigma, \theta; x, y, t)}{\partial x} + \frac{\partial c_{g,y} N(\sigma, \theta; x, y, t)}{\partial y} + \frac{\partial c_{\theta} N(\sigma, \theta; x, y, t)}{\partial \theta} + \frac{\partial c_{\sigma} N(\sigma, \theta; x, y, t)}{\partial \sigma} = \frac{S(\sigma, \theta; x, y, t)}{\sigma} \quad (1)$$

where $N(\sigma, \theta)$ is the action density spectrum; $C_{gx}, C_{gy}, C_{\theta}, C_{\sigma}$ are propagation velocities in x -, y -, θ - and σ - space respectively; $S(\sigma,$

θ) is the source term which could be represented as

$$S = S_{in} + S_{nl3} + S_{nl4} + S_{ds,w} + S_{ds,b} + S_{ds,br} \quad (2)$$

where the first term denotes the wind energy input, the second and third term represent the wave energy distribution through three-wave (triad) and four-wave (quadruplet) interactions, and the last three terms represent the wave energy dissipation caused by white-capping, bottom friction and depth-induced wave breaking. Details of the parameterization of these terms can be found in Booi et al. (1999, N. 2015).

2.2. Coastal circulation model

FVCOM is a prognostic, unstructured grid, finite-volume coastal ocean model (Chen et al., 2003). It uses non-overlapped triangular grids in the horizontal to resolve the complex shoreline and geometry, and the generalized terrain-following Sigma coordinate in the vertical direction. The present version of FVCOM (version 3.2.2) includes both hydrostatic and non-hydrostatic schemes (Lai et al., 2010a, 2010b) and wetting/drying treatment. The mode-split approach is used for the solution of the circulation model, in which currents are divided into external and internal modes and computed using an external and internal time step respectively (Chen et al., 2003).

2.2.1. Model equations

Following U10, the hydrodynamic model equations, including the Vortex Force formalism and (at right-hand side of equation) the newly included WEC terms, are given by:

$$\begin{aligned} \frac{\partial \mathbf{V}}{\partial t} + (\mathbf{V} \cdot \nabla_{\perp}) \mathbf{V} + w \frac{\partial \mathbf{V}}{\partial z} + f \hat{\mathbf{z}} \times \mathbf{V} + \nabla_{\perp} \phi \\ - \mathbf{F} - \frac{\partial}{\partial z} \left(K_M \frac{\partial \mathbf{V}}{\partial z} + \nu \frac{\partial \mathbf{V}}{\partial z} \right) = -\nabla_{\perp} \mathcal{K} + \mathbf{J} + \mathbf{F}^w \\ \frac{\partial \phi}{\partial z} + \frac{g\rho}{\rho_0} = -\frac{\partial \mathcal{K}}{\partial z} + K \\ \nabla_{\perp} \cdot \mathbf{V} + \frac{\partial w}{\partial z} = 0 \end{aligned} \quad (3)$$

In these equations the boldface typesets are used for horizontal vectors, while the vertical components are represented by a normal typeset so that 3D vectors are designated by (**horizontal**, vertical). (\mathbf{V} , w) and (\mathbf{V}^{st} , w^{st}) are the Eulerian mean and Stokes velocities, respectively; f is the Coriolis parameter; ϕ is the dynamic pressure (normalized by the density ρ_0); \mathbf{F} represents the non-wave non-conservative forces; \mathbf{F}^w represents the wave-induced non-conservative forces; (\mathbf{J} , K) is the Vortex Force and \mathcal{K} is the lower order Bernoulli head (after removing quasi-static terms, see Section 9.6 of MRL04); ρ and ρ_0 are total and reference densities of sea water respectively; g is the gravity acceleration; and ν_0 is the molecular diffusivity. An overbar represents time average, and a prime represents a turbulent fluctuating quantity. The vertical coordinate range is $-h(x) \leq z \leq \zeta + \hat{\zeta}$, in which ζ and $\hat{\zeta}$ are the mean and quasi-static sea level components, respectively. All wave quantities are referenced to the local wave-averaged sea level, $z = \zeta + \hat{\zeta}$, rather than the mean sea level, $z = 0$.

The three-dimensional Stokes velocity (\mathbf{V}^{st} , w^{st}) is defined for a spectral wave field as:

$$\mathbf{V}^{st}(z) = \frac{2E}{c} \frac{\cosh[2z]}{\sinh[2\mathcal{H}]} \mathbf{k} \quad (4)$$

$$w^{st}(z) = -\nabla_{\perp} \cdot \int_{-h}^z \mathbf{V}^{st} dz' \quad (5)$$

where E is the wave energy; c is the phase speed of the waves; \mathbf{k} is the wave number vector and k is its magnitude; $h(\mathbf{x})$ is the resting depth. \mathcal{Z} and \mathcal{H} are the normalized vertical lengths, defined as:

$$\mathcal{Z} = k(z + h); \text{ and } \mathcal{H} = k(h + \zeta + \hat{\zeta}) = kD \quad (6)$$

where $D = h + \zeta + \hat{\zeta}$ is the wave-averaged thickness of the water column. Finally, the wave energy E , phase speed c and intrinsic frequency σ are given by:

$$E = \frac{1}{16} g H_s^2; \quad c = \frac{\sigma}{k}; \quad \sigma = \sqrt{gk \tanh[\mathcal{H}]} \quad (7)$$

where H_s is the significant wave height.

The Vortex Force (\mathbf{J} , K) and the Bernoulli head term (\mathcal{K}) are expressed as:

$$\begin{aligned} \mathbf{J} &= -\hat{\mathbf{z}} \times \mathbf{V}^{st} (f + (\hat{\mathbf{z}} \cdot \nabla_{\perp} \times \mathbf{V})) - w^{st} \frac{\partial \mathbf{V}}{\partial z} \\ K &= \mathbf{V}^{st} \cdot \frac{\partial \mathbf{V}}{\partial z} \\ \mathcal{K} &= \frac{1}{32} \frac{\sigma H_s^2}{k \sinh^2[kD]} \int_{-h}^z \frac{\partial^2 \Upsilon}{\partial z'^2} \sinh[2k(z - z')] dz' \end{aligned} \quad (8)$$

where $\Upsilon = \mathbf{k} \cdot \mathbf{V}$, and $\hat{\mathbf{z}}$ is the unit vector in the vertical direction.

The quasi-static sea level component is expressed as:

$$\hat{\zeta} = -\frac{P_{atm}}{g\rho_0} - \frac{H_s^2 k}{16 \sinh[2\mathcal{H}]}, \quad (9)$$

in which an inverse barometric response to changes in atmospheric pressure P_{atm} and a phase-averaged set-up/set-down (with respect to the still water) are included.

For random waves, the wave energy E is replaced by the elementary variance, $E(\sigma, \theta) d\sigma d\theta$, and the entire expressions (e.g. Eq. (4)) are integrated over the spectrum of the relative frequencies and angles of wave propagation of the wave model. It should be noted that, the expression of Stokes drift (Eq. (4)) in strongly nonlinear waves can be different from the second-order approximation (Grue and Kolaas, 2017), which is outside the scope of the present study.

With the additional WEC terms on the right-hand side, the boundary conditions for the newly developed model are expressed as:

$$\begin{aligned} w|_{-h} + \mathbf{V}|_{-h} \cdot \nabla_{\perp} h &= 0 \\ w|_{\zeta + \hat{\zeta}} - \frac{\partial \zeta}{\partial t} - (\mathbf{V}|_{\zeta + \hat{\zeta}} \cdot \nabla_{\perp}) \zeta \\ &= \nabla_{\perp} \cdot \overline{\mathbf{V}^{st}} + \frac{\partial \hat{\zeta}}{\partial t} + (\mathbf{V}|_{\zeta + \hat{\zeta}} \cdot \nabla_{\perp}) \hat{\zeta} \\ g \zeta - \phi|_{\zeta + \hat{\zeta}} &= \mathcal{P} \end{aligned} \quad (10)$$

where $\overline{\mathbf{V}^{st}}$ is the depth-averaged Stokes velocity and \mathcal{P} is the wave-averaged forcing surface boundary condition, defined as:

$$\begin{aligned} \mathcal{P} &= \frac{gH_s^2}{16\sigma} \left\{ \frac{\tanh[kD]}{\sinh[2kD]} \left(-\frac{\partial Y}{\partial z} \Big|_{\zeta + \hat{\zeta}} + \cosh[2kD] \frac{\partial Y}{\partial z} \Big|_{-h} \right. \right. \\ &\quad \left. \left. + \int_{-h}^{\zeta + \hat{\zeta}} \frac{\partial^2 Y}{\partial z'^2} \cosh[2kz'] dz' \right) - 2k \tanh[kD] Y \Big|_{\zeta + \hat{\zeta}} \right\} \end{aligned} \quad (11)$$

2.2.2. Parameterization of non-conservative wave acceleration, \mathbf{F}^w

The non-conservative wave acceleration/forcing term, \mathbf{F}^w , originates from the fact that surface gravity waves lose energy when propagating towards the shoreline. This phenomenon includes three different dissipation processes: (a) white-capping (ε^{wcap}); (b)

depth-induced wave breaking (ε^b); and (c) bottom friction (ε^{bf}). Thus \mathbf{F}^w is expressed as:

$$\mathbf{F}^w = \mathbf{B}^{wcap} + \mathbf{B}^b + \mathbf{B}^{bf} + \mathbf{B}^{sf} \quad (12)$$

where \mathbf{B}^{wcap} is the white-capping induced acceleration; \mathbf{B}^b contains both the depth-induced breaking (\mathbf{B}^{db}) and roller accelerations (\mathbf{B}^r); \mathbf{B}^{bf} and \mathbf{B}^{sf} denote accelerations due to bottom and surface streaming, respectively. These accelerations could either be represented as body forces, or as equivalent boundary stresses for the cases in which the associated turbulence boundary layers are too thin to be resolved. For a detailed parameterization of these terms, the reader is referred to the [Appendix A](#).

2.2.3. Wave-enhanced bottom drag

The interactions of waves and currents in the bottom boundary layer can affect the hydrodynamics results in coastal circulation modeling, particularly in the surf zone. In order to parameterize the wave enhanced bottom shear stress, the drag law proposed by [Soulsby \(1995\)](#) is used here in the coupled model system:

$$\tau_{bot}^{cd} = \tau_c \left[1.0 + 1.2 \left(\frac{|\tau_w|}{|\tau_w| + |\tau_c|} \right)^{3.2} \right] \quad (13)$$

$$\tau_c = \rho_0 \left[\frac{\kappa}{\ln(z_m/z_b)} \right]^2 |\bar{\mathbf{V}}| |\bar{\mathbf{V}}|; |\tau_w| = \frac{1}{2} \rho_0 f_w |\bar{\mathbf{V}}_{orb}^w|^2 \quad (14)$$

where τ_c and τ_w are bottom stresses due to current and waves; $\kappa = 0.4$ is the von Kármán constant; z_m is a reference height above the bed, nominally equivalent to half the height of the first grid cell above the bed (in a barotropic model $z_m = D/2$; e.g. [Uchiyama et al., 2009](#)); z_b is the bed roughness length; f_w is the wave friction factor given by

$$f_w = \text{Min} \left\{ 0.3, 1.39 \left(\frac{A_b}{z_b} \right)^{-0.52} \right\}; \quad (15)$$

$$A_b = \frac{|\bar{\mathbf{V}}_{orb}^w|}{\sigma} = \frac{|\bar{\mathbf{V}}_{orb}^w|}{2\pi} T_{orb}^w = \sqrt{2 \int_0^{2\pi} \int_0^\infty \frac{1}{\sinh^2 kd} E(\sigma, \theta) d\sigma d\theta} \quad (16)$$

$|\bar{\mathbf{V}}_{orb}^w|$ is the bottom wave orbital velocity and T_{orb}^w is the near bottom wave period defined as the ratio of the bottom excursion amplitude to the root-mean-square velocity $T_{orb}^w = \sqrt{2\pi} A_b / U_{rms}$.

2.3. Wave-enhanced vertical turbulent mixing

Wave breaking leads to extra turbulence generation at the surface and enhances turbulent kinetic energy (TKE) levels in the water column ([Thorpe, 1984](#); [Agrawal et al., 1992](#); [Moghimi et al., 2016](#)). [Craig and Banner \(1994\)](#) accounted for this effect by implementing a new flux-type surface boundary condition for the TKE in a one-dimensional M-Y2.5 turbulence closure model. This approach has been implemented in the present study for incorporating the effects of wave breaking on vertical mixing, by adapting a generic length scale (GLS) two-equation turbulence closure model similar to approaches by [Burchard et al. \(1999\)](#) and [Umlauf et al. \(2005\)](#).

The GLS model, introduced by [Umlauf and Burchard \(2003\)](#), has been tested against measurements for oscillating grid generated turbulence which is considered to be similar to the wave-breaking induced turbulence. However, the original GLS model is modified in the present study to better account for the wave-enhanced vertical mixing. The two equations for k and for the GLS (ψ) read:

$$\frac{\partial k}{\partial t} + \mathbf{V} \cdot \nabla k = \frac{\partial}{\partial z} \left(\frac{K_M}{\sigma_k} \frac{\partial k}{\partial z} \right) + P + B - \varepsilon$$

$$\frac{\partial \psi}{\partial t} + \mathbf{V} \cdot \nabla \psi = \frac{\partial}{\partial z} \left(\frac{K_M}{\sigma_\psi} \frac{\partial \psi}{\partial z} \right) + \frac{\psi}{k} (c_1 P + c_3 B - c_2 \varepsilon F_{wall}) \quad (17)$$

where $P = K_M [(\frac{\partial u}{\partial z})^2 + (\frac{\partial v}{\partial z})^2]$ and $B = K_H \frac{g}{\rho_0} \frac{\partial \rho}{\partial z}$ represent the turbulence production rates by shear and buoyancy, respectively; K_M and K_H are the vertical eddy viscosity and vertical eddy diffusion coefficients, respectively; $\varepsilon = (c_\mu^0)^3 k^{3/2} l^{-1}$ is the turbulence dissipation rate; σ_k and σ_ψ are the turbulent Schmidt numbers for k and ψ , respectively; F_{wall} is a wall function; and C_1 , C_2 and C_3 are coefficients which can be found in [Warner et al., \(2005\)](#). The GLS (ψ) is defined as:

$$\psi = (c_\mu^0)^p k^m l^n \quad (18)$$

where c_μ^0 is the stability coefficient based on experimental data for non-stratified channel flow, it takes on a specific value when used with a stability function and other model parameters ([Warner et al., 2005](#)); $p=2.0$, $m=1.0$ and $n=-0.67$ are coefficients, following suggestions by [Umlauf and Burchard \(2003\)](#). Note that many conventional turbulence schemes can also be derived from this GLS model by using specific combinations of values for p , m and n (e.g. a $k\varepsilon$ scheme is reproduced by $p=3$, $m=1.5$ and $n=-1.0$; a $k\psi$ scheme is reproduced by $p=-1.0$, $m=0.5$ and $n=-1.0$).

The TKE injection due to wave breaking is provided by a boundary condition at the water surface ([Craig and Banner, 1994](#); [Feddersen, 2012a, 2012b](#)):

$$F_k = \frac{K_M}{\sigma_k} \frac{\partial k}{\partial z} \Big|_{z^c} \quad (19)$$

where F_k is the surface flux of energy injected into water column, which can be either parameterized in proportion to the cube of surface wind friction velocity ([Craig and Banner, 1994](#)) as $F_k = c_w (u_*^s)^3$, or directly obtained from a surface wave model as a fraction of the surface wave dissipation, i.e. $F_k = b_w [(1 - \alpha_r) \varepsilon^b + \varepsilon^r + \varepsilon^{wcap}]$; where u_*^s is the surface friction velocity and c_w and b_w are empirical constants. The former formulation has been used at deep seas and open seas ([Craig, 1996](#); [Terray et al., 1996](#)) with $c_w \approx (100 \sim 150)$, while the latter formulation is more appropriate in the surf zone. The $b_w (\approx 0.01 \sim 0.25)$ is used for depth-induced breaking ([Govender et al., 2004](#); [Huang et al., 2009](#); [Feddersen and Trowbridge, 2005](#); [Feddersen, 2012a, 2012b](#)) and $b_w \approx 1$ is for deep water white-capping ([Bakhoday Paskyabi et al., 2012](#)).

Neumann-type surface boundary conditions for k and ψ (following [Umlauf and Burchard, 2003](#)) are applied at vertical position of z' :

$$\frac{K_M}{\sigma_k} \frac{\partial k}{\partial z} = -\frac{c_\mu}{\sigma_k} (\mathbb{K})^{\frac{3}{2}} L \cdot \alpha (z_0 - z')^{\frac{3}{2}} \alpha$$

$$\frac{K_M}{\sigma_\psi} \frac{\partial \psi}{\partial z} = -\frac{c_\mu (c_\mu^0)^p}{\sigma_\psi} (m\alpha + n) (\mathbb{K})^{m+\frac{1}{2}} L^{n+1} (z_0 - z')^{(m+\frac{1}{2})\alpha+n} \quad (20)$$

where α is the spatial decay rate of TKE in the wave-enhanced layer; L is the slope of the turbulent length scale; $\mathbb{K} = (-\frac{\sigma_k}{c_\mu \alpha} F_k)^{\frac{2}{3}} \frac{1}{z_0}$ and F_k is the injection flux of TKE at the water surface.

In the present study, the surface roughness z_0 is connected to the length scale of injected turbulence which is determined uniquely by the spectral properties of turbulence at the source. This parameter directly affects the vertical distribution of TKE in the upper portion of the water column ([Moghimi et al., 2016](#)). However, due to the difficulty in measuring this parameter, a wide range of values have been proposed (e.g. [Craig and Banner, 1994](#); [Terray et al., 1999](#); [Umlauf et al., 2003](#); [Stips et al., 2005](#); [Feddersen and Williams, 2007](#); [Moghimi et al., 2016](#)). In the present study, $z_0 = \alpha_w H_s$, where α_w is kept as a tuning parameter which is adjusted to produce results closest to the available observations.

3. Numerical implementation in FVCOM

3.1. Model solution method

Prior to implementing into the modeling system, the model equations are firstly expressed in a flux-divergence form where several new variables are further defined, and then transformed from the Cartesian (x, y, z, t) coordinate system into the Sigma (x, y, s, t) coordinate system. These procedure steps are inspired by U10, but are kept to be more appropriate for FVCOM. For a detailed description, the reader is referred to the [Appendix B](#).

The model domain is discretized using unstructured mesh made up by no-overlapping triangle elements. For the circulation model, the scalar variables (e.g. $\zeta^c, H, D, w^i, K_m, K_h$) are placed at vertices while u and v are placed at centroids, where the model differential equations are solved with the similar numerical scheme as that used in the original FVCOM ([Chen et al., 2003](#)). The same set of triangular mesh is also used for the wave module to avoid the interpolation between different sets of computational grids. The wave action balance equation (1) is integrated over the vertices of the triangular grids by a point-to-point multi-directional Gauss–Seidel iteration technique ([Zijlema, 2010](#)). This locally implicit but globally explicit numerical approach circumvents the need to build or store large matrices by taking advantage of the newly acquired vertex values during an iteration. Consequently, the numerical procedure remains stable at large time step and can converge to a steady state much more rapidly than explicit methods, while being more computationally efficient than implicit methods ([Zijlema, 2010](#); [N. Booij et al., 2015](#)).

The code of this new model system has also been parallelized for running on High Performance Computing clusters. Similar to the original FVCOM model, the METIS library is used to partition the global unstructured model mesh and the Message Passing Interface (MPI) distributed memory parallelism communication protocol is used to exchange information between adjacent processors.

3.2. Coupling of the wave and circulation models

The original FVCOM and Un-SWAN are two separate models with very different codes structures. Many efforts are therefore made to couple these two models into one system. Generally speaking, the FVCOM model is used as the main control programme and the Un-SWAN is merged into the FVCOM model suit as sub-programme. In this process, many necessary modifications to the original code and development of new modules are carried out in order to make the two models to be consistent with each other. To facilitate data exchange between these two models, a new coupler module is also developed based on a two-way coupling scheme, similar to the approach employed by FVCOM-SWAVE ([Wu et al., 2011](#)). Due to the implicit scheme used in the Un-SWAN, the wave propagation time step could be generally much larger than the circulation time step. Therefore, the coupling interval is designed to be the same as the wave propagation time step, which is specified as a multiple of the internal time step of the circulation model. In the following tests, however, the default wave time step is taken as the same as internal time step of the circulation model for simplicity reason.

At the beginning of the defined coupling cycle, the wave model runs first, with the specific sea surface elevation, current fields and bathymetric changes that obtained directly from the circulation model at the end of previous cycle, to compute the required wave parameters, e.g. wave height, wave direction, wave relative peak period, wave bottom orbit velocity and wave dissipation variance. Based on these updated information, the coupler module then calculates the relevant WEC terms, including non-conservative wave accelerations, wave friction factor, which are then passed to

the circulation model to solve the hydrodynamic variables. With these WEC terms, the circulation model runs several time steps to the end of this coupling cycle and provides data for solving the wave model at the next time interval, marks the end of a coupling cycle of wave and current models.

The wave and circulation models utilize the same set of global triangular mesh. However, two different sets of local sub-meshes, i.e. element-based sub-meshes for the circulation model ([Chen et al., 2003](#); [Wang and Shen, 2011](#)) and vertex-based sub-meshes ([Dietrich et al., 2011](#)) for the wave model, are employed in the adopted parallel coupling scheme in the present study. This is determined by the different intrinsic characteristics of these two models, e.g. the locations (centroids or vertexes) of variables, discretization technique (finite volume or finite difference method) for partial differential equations. Therefore, when inter-model communication is needed during the parallel running, the information from one set of local sub-mesh (element-based/vertex-based) is firstly collected by the master processor into the global mesh and then distributed into another sub-mesh (vertex-based/element-based). Such a procedure is designed to exchange information between these two local sub-meshes as effectively as possible.

4. Model validation

The new model system is firstly validated against analytical solution for obliquely incident waves break on a constant mild sloping (1/80) planar beach. This test case was initially posed by HW09 and later used as benchmark in a series of numeric studies using different wave-current interaction approaches, e.g. the depth-dependent Radiation Stress formulation (HW09; [N. Kumar et al., 2011](#)), the Vortex Force formulation (U10; K12) and the glm2z-RANS theory ([Michaud et al., 2012](#)).

The model domain covers a 1900 m long (cross-shore) by 300 m wide (alongshore) rectangular area, which is discretized using isosceles right triangles with grid size of 20 m in the horizontal and 31 vertical sigma levels with uniform thickness, resulting in a total of 1536 nodes and 2850 elements. It has a west-east orientation with the offshore boundary open boundary located at $x = 100$ m. The water depth varies from 12 m below the still water level at the offshore boundary to 0.75 m above at the shoreline. The boundary conditions include periodic boundaries in the along-shore direction, wetting/drying at the shoreline, and a clamped water level boundary condition ([Chen et al., 2003](#)) at the offshore boundary. Coriolis forces are excluded, and there is no lateral momentum diffusion, stratification, and surface wind/heat/freshwater fluxes. The roller waves and bottom streaming effects are also not included. The bottom stress is formulated using the quadratic bottom drag with a constant c_d value of 0.0015. The wave information is provided at the offshore boundary based on a JONSWAP spectrum with 2 m significant wave height, 10 s peak wave period and a 10° angle of incidence. Both the barotropic and baroclinic time step in the standard test case is 0.1 s, whose results are used for the analysis in [Sections 4.1 and 4.2](#).

For this condition, [Uchiyama et al. \(2009\)](#) showed that the barotropic continuity balance can be integrated in the cross-shore direction to yield a balance between depth-averaged Eulerian and Stokes velocities, i.e. $\bar{u} = -\bar{u}^{st}$. In addition, a dominant cross-shore barotropic momentum balances between the pressure gradient force (PGF) and breaking acceleration, i.e.

$$\rho_0 g \frac{\partial (\zeta^c - \hat{\zeta})}{\partial x} = \frac{\varepsilon^b k_x}{D\sigma} \quad (21)$$

and an alongshore momentum balance between bottom drag and breaking acceleration, i.e.

$$\rho_0 c_d |\bar{\mathbf{V}}| \bar{v} = \frac{\varepsilon^b k_y}{\sigma} \quad (22)$$

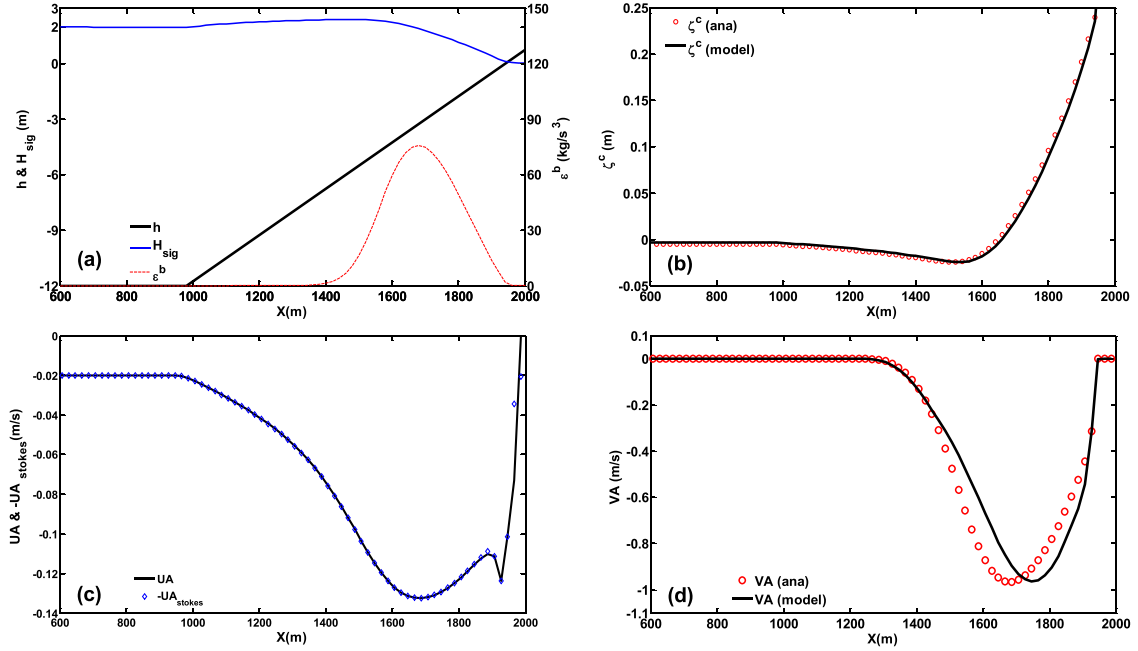


Fig. 1. Simulation results and analytical solutions of the obliquely incident waves on a plane beach test case. Cross-shore distribution of (a) significant wave height H_{sig} , depth h and breaking dissipation rate ϵ^b ; (b) sea surface elevation ζ^c ; (c) depth-averaged cross-shore Eulerian velocity UA (solid line) and Stokes velocity $-UA_{Stokes}$ (blue diamonds); and (d) longshore velocity VA . (For interpretation of the references to color in this figure legend, the reader is referred to the web version of this article).

can be obtained; where $\vec{V} = \sqrt{\bar{u}^2 + \bar{v}^2}$. Along with the wave parameters and wave breaking induced dissipation (ϵ^b) produced by the Un-SWAN, Eqs. (21) and (22) can be solved to obtain the analytical solutions for \vec{V} and $\zeta^c(x)$.

4.1. Wave parameters and two-dimensional fields

The computed cross-shore distributions of significant wave height, depth-induced breaking dissipation and water depth are shown in Fig. 1a. When propagating across the slope, waves shoal between $x = 1000$ m and 1400 m and begin to break around $x = 1400$ m (indicated by the increase in breaking dissipation ϵ^b in Fig 1a). The wave energy dissipation rate remains zero during wave shoaling and has a maximum value of 75 kg/s^3 at about $x = 1700$ m, which is identical to results in U10 and K12. The computed free surface ζ^c (solid line in Fig. 1b) gradually decreases landward from a small negative value at the offshore boundary to a maximum wave set-down at about $x = 1500$ m, where it then increases monotonically to a maximum wave setup of approximately 0.22 m at the shoreline. These results agree very well with the analytical solutions shown in Fig 1b.

The predicted depth-averaged cross-shore Eulerian flow (solid line in Fig. 1c) has equal magnitude and opposite sign to the depth-averaged Stokes flow (red circle in Fig. 1c), i.e. is in perfect agreement with $\bar{u} = -\bar{u}^{st}$. The depth-averaged longshore-shore velocity attains a maximum value of approximately 0.93 m/s at about $x = 1750$ m and decreases to zero towards the shoreline and offshore, which also agrees well with previous studies (U10; Kumar et al., 2011; K12). Because of a cross-shore momentum imbalance associated with the non-conservative wave accelerations and wave-enhanced vertical mixing (U10), the maximum value of the longshore-shore velocity is shifted shoreward compared to the analytical solution (Eq. (22), red circle in Fig. 1d).

4.2. Three-dimensional velocities

The vertical structure of the simulated Eulerian mean and Stokes velocities are shown in Fig. 2. Inside the surf zone ($x >$

1400 m; Fig. 2a), the Eulerian mean cross-shore velocity shows a strong recirculation cell with velocities directed onshore near the water surface and directed offshore close to the sea bed. The longshore velocity attains the maximum value at the water surface and decreases slightly towards the sea bed, with a maximum value of approximately -1 m/s throughout the domain located at about $x = 1750$ m. Outside the surf zone ($x < 1400$ m) the cross-shore velocity is weak in magnitude, directed offshore and almost uniform over depth, and also the longshore velocity is much weaker throughout the entire water column.

Near the sea surface, the computed cross-shore Stokes velocity (Fig. 2c) increases from near zero at the offshore boundary and the shoreline to a maximum value of ~ 0.15 m/s at the location of maximum wave breaking (i.e. $x = 1700$ m). Vertically, the velocity decreases from the sea surface towards the sea bed. The longshore Stokes velocity (Fig. 2d) follows a similar distribution as the cross-shore Stokes velocity, but is about one order of magnitude weaker in strength because of the relatively small wave obliqueness.

The model results clearly follow the analytical solution for this particular condition and are consistent with previous similar research work in U10 and K12 despite different turbulence closure schemes being used in these models. This demonstrates the model's capability and accuracy for simulating coastal surface wave induced currents.

4.3. Model convergence

Roland and Ardhuin (2014) indicated that large time step could affect the convergence of SWAN solution. To test the effects of the time steps on the module solution, five sensitivity tests with increased time steps are carried out, see Table 1. These tests are based on the same model setup as above validation case. All tests are run with the nonstationary mode of Un-SWAN, start from 00:00:00 until convergent results are obtained. The model convergence time (Table 1) is defined as the time when the normalized root means square error of wave height (WHNRMS) is less than 1.0%. The WHNRMS is defined as $\epsilon_j = \left\{ \frac{\sum_{i=1}^{NodeNum} (hs_{i,j} - hs_{i,0})^2}{\sum_{i=1}^{NodeNum} (hs_{i,0})^2} \right\}^{1/2}$, in

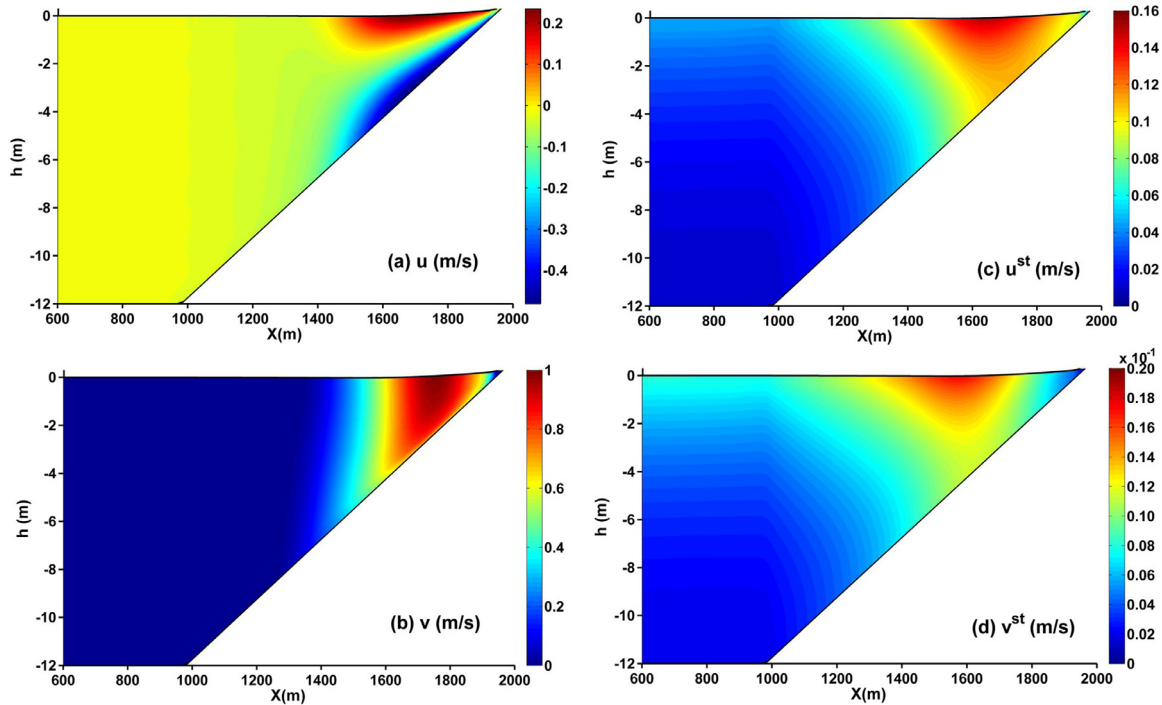


Fig. 2. Cross-shore section of Eulerian and Stokes velocities from the simulation. (a) cross-shore (u); (b) longshore (v); and (c) cross-shore (u^{st}) and (d) longshore (v^{st}).

Table 1

Wave time step and convergence time of 6 test cases.

Test case #	#0 (standard case)	#1	#2	#3	#4	#5
Wave time step (s)	0.1	1.0	10.0	100.0	1000.0	10,000.0
Convergence time (hh:mm:ss)	00:05:00	00:05:15	00:08:40	00:43:20	06:56:40	69:26:40
Convergence steps	3000	315	52	26	25	25

which hs_{i0} represent the convergent wave height simulated in the standard case and hs_{ij} represent the wave height of test case j ($j=1,2,3,4,5$). It can be seen that the model convergence time of these six tests in Table 1 increases monotonously with increase time steps, which verifies that the Un-SWAN in the present study is able to remain stable and converge into a steady state at these given time step sizes.

The convergence steps in Table 1, defined as $\frac{\text{Convergence Time}}{\text{Wave Time Step}}$, reduce firstly as time step increases but then remain approximately constant when the wave time step is larger than 100 s. The computational efforts are much less for the cases with large time steps and fewer convergence steps, in comparison with the cases with small time step and large number of convergence steps. On the other hand, the time step in the circulation model is unavoidably limited by the CFL criterion. For a given time step in the circulation model, a large time steps in the wave model means more internal mode calculations are required in the circulation model, which will increase the computation load. Therefore, when the whole coupled model system is implemented in practise, the time step for the wave model should be decided for the optimal operation for both wave and current models. In the present study, a 10 s is used as typical time step for the following cases.

Two tests with different spatial resolutions, i.e. 5 m (run 6), 50 m (run 7), are also carried out. Due to the large mesh size, the results in run 7 cannot capture all the characteristics. The difference between the results of run 6 and the base case run 0 are very small. Therefore, a spatial resolution of 20 m is considered sufficient for this test case.

5. Model applications

After validation, the model was applied to several complex cases with detailed measurements to test its efficiency and to examine the details of hydrodynamics under breaking waves on a beach at very different scales. More importantly, the effects of wave breaking induced turbulence on the flow structure can be revealed through the newly implemented turbulence model.

Three test cases are described in detail. The first case reproduces the breaking wave characteristics, wave-induced undertow and turbulence structures as measured in high detail around a fixed breaker bar during a recent laboratory experiment. In the second case, the model system is applied to simulate field-scale measurements conducted during the DUCK94 experiment (e.g. Garcez Faria et al., 1998, 2000), in which wave-induced undertow as well as alongshore currents are studied and further analyzed through momentum balance. As these two cases largely focus on conditions of (approximate) alongshore uniformity, the third case involves a laboratory experiment conducted on a beach with a shore-parallel breakwater, which introduces three-dimensionality in the domain and flow development. This case examines the model's ability of simulating complex three-dimensional flow around structures in coastal regions with desirable flexibility in the unstructured mesh.

5.1. Wave breaking over breaker bar at laboratory scale

Breaking wave characteristics over a barred profile can be significantly different from those on a plane sloping beach (Smith and Kraus, 1991), and consequently the wave-induced velocities and

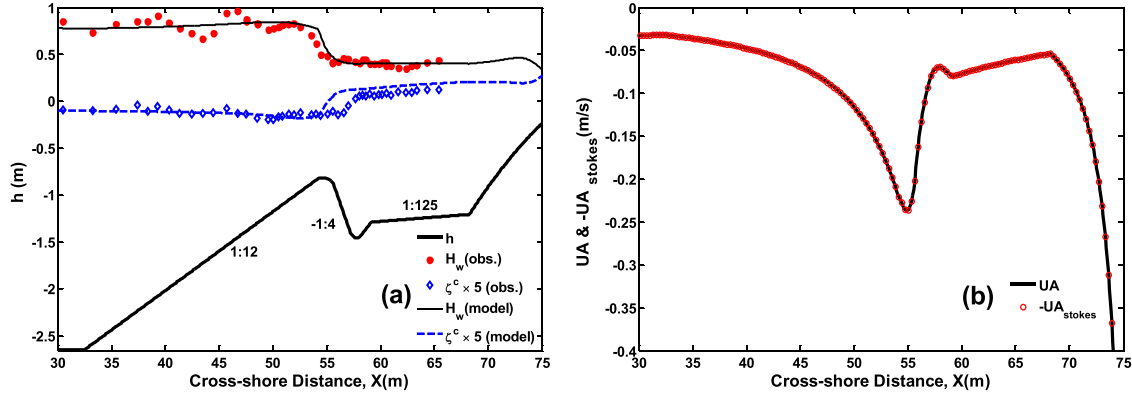


Fig. 3. Simulated and measured results of the large-scale breaking wave experiment with a naturally shaped breaker bar. Cross-shore distribution of (a) significant wave height H_{sig} and five times of sea surface elevation $\zeta^c \times 5.0$; (b) depth-averaged cross-shore Eulerian velocity UA (solid line) and Stokes velocity $-UA_{stokes}$ (red circles). (For interpretation of the references to color in this figure legend, the reader is referred to the web version of this article).

turbulence will also differ considerably. Recently, hydrodynamics and sand transport processes were measured under a large-scale plunging breaking wave during a combined laboratory campaign involving experiments with a mobile medium-sand bed (van der Zanden et al., 2016) and with a rigidized fixed bed (van der A et al., submitted). Both campaigns involve the same wave conditions and barred beach profile, which developed from an initially flat horizontal test section. The numerical model is validated against measurements of hydrodynamics, including turbulence, obtained with high spatial coverage during the fixed-bed experiment.

Fig. 3a shows the layout of the beach profile in the fix bed experiment, consisting of a 1:12 offshore slope, a 0.6 m high breaker bar (measured from crest to trough) with a lee-side slope of approximately 1:4, followed by a 10 m long 1:125 slope and terminated by a fixed sloping beach. Regular waves ($H = 0.85$ m and $T = 4$ s) were generated at offshore boundary with a 2.65 m water depth by a wedge-type wave paddle. The water surface elevations, used to quantify the wave height and mean surface elevation, were measured with sidewall-mounted resistive wave gauges at 19 locations covering the deep part of the flume to the shoaling zone and were measured with pressure transducers at 37 locations for the remainder of the flume (i.e. at the breaking and inner surf zones). Instantaneous velocities were measured at 12 cross-shore locations along the bar region, covering the shoaling, breaking and inner surf zones, using a Laser Doppler Anemometer (LDA) and two Acoustic Doppler Velocimeters (ADV) deployed from a mobile frame. Velocities were measured over the entire water column with a vertical measurement separation distance of 0.10 m. The instantaneous velocities were decomposed into a time-averaged, wave-related and turbulent component, following a Reynolds decomposition. Further details on the measurements and data processing can be found in van der A et al. (2017).

The corresponding model domain covers an area of 70 m in the cross-shore by 1 m in the longshore direction. The spatial resolution is 0.1 m in both directions, together with equally spaced 33 vertical sigma layers, yielding a total of 14,000 elements. The water depth at the offshore boundary is fixed at 2.65 m in accordance with the experiment. At the offshore boundary, the model is forced with regular normally incident waves with a 4 s period and 0.85 m wave height. In this study, the original code of Un-SWAN is further developed to allow the simulation of normally incident regular waves, by limiting the wave propagation direction in exactly one direction bin, e.g. zero degree in this case, and one frequency bin. The recently developed β -kd approach in Salmon et al. (2015) is chosen to account for the depth-induced wave breaking, as the numerical results improved significantly compared to that from the more widely used constant breaker index approach. Following the

baseline numerical experiment of U10, the shape function of Eq. (A3) with $a_b = 0.2$ and of Eq. (A19) with $a_{bf} = 3.0$ are used for $f^b(z)$ and $f^{bf}(z)$, respectively. Bottom stress due to the combined action of waves and currents is estimated using the formulation proposed by Soulsby (1995) with $z_b = 0.001$ m which is representative for the roughness of the concrete rigidized bed. In order to obtain smooth solutions, a weak horizontal momentum diffusion coefficient of the order $0.10 \text{ m}^2/\text{s}$ is applied. The effect of wave rollers is considered in the simulation, with the roller evolution model (Eq. (A7)) fed by the wave dissipation obtained from the Un-SWAN wave module using $\alpha_r = 0.75$. $\alpha_w = 0.3$ and $b_w = 0.01$ are chosen for a proper description of the turbulence under breaking waves.

Starting from still water, a standard simulation of this test condition lasts for 30 min after which the results are found to be in hydrodynamic equilibrium using a barotropic and baroclinic time step of 0.01 s and 0.1 s respectively.

5.1.1. Wave height and water surface elevation

Fig. 3a compares the model computed and measured wave height and mean water level. After propagating from the offshore boundary into the model domain, it can be seen that the wave height decreases first due to the bottom friction induced wave attenuation and then increases gradually due to wave shoaling along the offshore bar slope. A maximum wave height is reached at $x \approx 52$ m, where depth-induced wave breaking occurs, resulting in a rapid decrease in wave height. Overall the model computed wave height agrees well with the measurements in the breaking area and inner surf zone (i.e. $x > 52$ m), although the model predictions of the breaking point and the strong decrease in wave height are shifted by about 1 m shoreward compared to the measurements. In the deeper section of the flume and along the offshore bar slope, the oscillation in the measured wave height is due to wave reflection and/or spurious wave generation in the laboratory, which is not seen in the modeled results. A factor of 5.0 was multiplied with mean water level to facilitate the inter-comparisons of the simulation and observation. The simulated mean water level shows a continuous and near constant set-down of approximately 2.5 cm from $x = 0$ m (i.e. the offshore boundary) to $x \approx 55$ m, where it rapidly (within 1 m) turns into a set-up. The set-up value increases slowly throughout the inner surf zone, with a maximum value of about 3.5 cm at the end of the flume. The cross-shore behavior and the quantitative set-down and set-up computed by the model are in good agreement with the measurements. However, a spatial lag of about 2 m is found in the simulated location where set-down changes to setup. This is closely related to the discrepancies of simulated wave breaking energy here (Eq. (21)), which in turn result from the overestimation of the wave height.

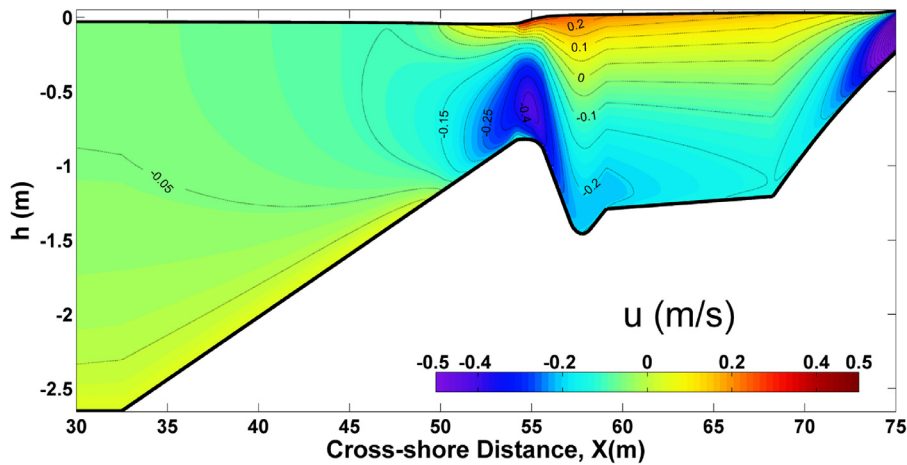


Fig. 4. Model simulated distribution of cross-shore velocity u in the large-scale wave flume experiment with a naturally shaped breaker bar; contour lines explicitly show the velocity value.

5.1.2. Velocities

The simulated depth-averaged Eulerian velocity as shown in Fig. 3b complies well with the barotropic mass conservation law which, similar to the characteristic shown in Fig. 1c, has the same magnitude but opposite sign to the depth-averaged Stokes flow. The simulated cross-shore and vertical distribution of Eulerian velocity in Fig. 4 is much more complicated than for the plane beach condition (Fig. 2) due to the more complex barred bathymetry. From the offshore boundary until $x = 51$ m, the Eulerian velocities are offshore-directed over the entire water column with relatively small magnitudes ($x < 0.10$ m/s) and are near uniform in cross-shore and vertical direction. In the remainder of the flume (i.e. $x > 51$ m) current velocities increase in magnitude. Large onshore-directed velocities occur near the water surface due to the enhanced mass flux related to depth-induced wave breaking and wave roller effects (see details below). These velocities are balanced by a return flow (undertow) in the bottom part of the water column, leading to strong vertical shear. Maximum onshore velocities, reaching values of 0.3 m/s, are located above the breaker bar, while maximum undertow velocities occur near the shoreline and above the breaker bar with values of about -1.4 m/s and -0.4 m/s respectively.

Eq. (A10) suggests that the total wave dissipation, which induces a shear stress at the water surface, equals $\varepsilon^{tot} = (1 - \alpha_r)\varepsilon^b + \varepsilon^r + \varepsilon^{wcap}$ where α_r controls the fraction of the breaking waves turned into wave rollers that propagate toward the shore before dissipating. The value of α_r (between 0 and 1) can change the rate of wave dissipation which in turn reshapes the velocity profile inside the surf zone. In order to give an explicit presentation of the effect of the wave roller, five different numerical experiments are conducted with α_r values equal to 0, 0.25, 0.5, 0.75 and 1.0. The simulated profiles of velocity for different α_r values are shown in Fig. 5a, which also includes the measured velocities. With $\alpha_r = 0$, the simulated velocity shows a strong vertical shear on the breaker bar and along the offshore slope, due to a strong onshore flow near the water surface as well as a large undertow, while above the bar trough and further inshore the simulated velocities are nearly depth-uniform and onshore and offshore time-averaged velocity magnitudes are much lower. The resulting vertical shear overestimates the measured shear above the breaker bar. As the value of α_r progressively increases from 0 to 0.75, the computed velocity profiles tend to follow the measurements better, i.e. the velocity shear gradually decreases on the breaker bar and above the offshore slope while it increases in the bar trough and further shoreward. However, when $\alpha_r = 1$ the

simulated near surface velocities above the offshore slope of the breaker bar are too small in comparison with the measurements, while the improvement of vertical velocity structures in the bar trough and further shoreward is minor. Overall, the model results with the α_r value of 0.75 show the best agreement with the measured data in these five simulations as shown in Fig. 5b and hence is used in this study. However, the local best fit value of α_r shows in Fig. 5a is different at different cross-shore locations, which suggests that α_r is more appropriate to be regarded as a function of the cross-shore positions (i.e. a function of local bathymetry slope and/or local wave characteristics) in the surf zone. The results demonstrate that the inclusion of wave roller effects improve the model performance significantly.

Although Fig. 5b shows a good agreement between the simulated and the measured Eulerian velocities, it is also noted that the simulated undertow is apparently underestimated along the steeper shoreward slope of the breaker bar (i.e. $x = 56$ m and 56.5 m), which is most likely caused by the underestimated surface wave dissipation and overestimation in wave height around the breaker bar (Fig. 3a). To verify the guess, an additional simulation with locally enhanced wave dissipation (i.e. ε^b in Eq. (A4)) in this region ($x = 56$ m to 57 m) was conducted. As shown in Fig. 5c, this leads to a much better agreement with the measurements.

5.1.3. Turbulent kinetic energy

The model computed TKE is also compared with the measurements at the same 12 profiles (Fig. 6a). Overall, fairly good simulation results are obtained except at the profile of 3–5 around the breaking point, where TKE is obviously over-predicted. Note that over-predictions of TKE in the breaking region have been reported in many 2D and 3D simulations using various turbulence closure models (Xie, 2013; Brown et al., 2016). Various explanations for this overestimating have been given, e.g. the omission of TKE contained in the overturning jet during wave breaking (Lin and Liu, 1998), the exclusion of air effects on turbulence production and dissipation before the impingement of the overturning jet (Christensen et al., 2002), the exclusion of air bubbles in conventional turbulence models (Xie, 2013), and the invalidity of the turbulence model coefficients, that have been calibrated for quasi-steady turbulent flows rather than wave-induced oscillatory flows with strong free surface dynamics (Lin and Liu, 1998; Shao, 2006).

We conjecture an underestimated turbulence dissipation rate as the main cause of the over-prediction of TKE around the breaking point, which is likely due to inappropriate coefficients in the

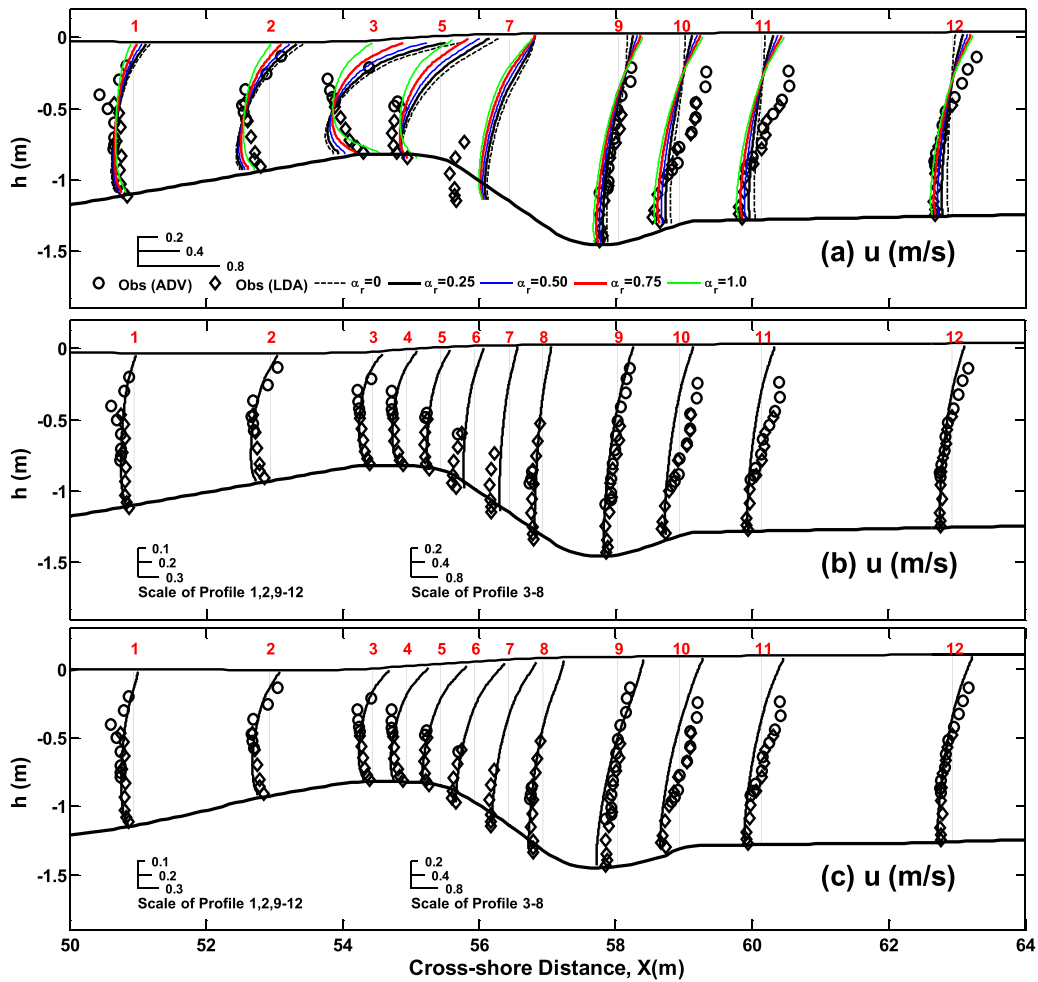


Fig. 5. Comparison of simulated (lines) with observed vertical profiles (circles and diamonds) for cross-shore velocities. (a) five simulations with $\alpha_r = 0.0, 0.25, 0.50, 0.75, 1.0$; (b) the standard run with $\alpha_r = 0.75$; (c) the run with local enhanced wave dissipation at $x=56-57\text{ m}$; The vertical dashed lines indicate the profile measurement locations and zero value for each profile.

turbulence model. Therefore, four sensitivity simulations are conducted with a variation of the coefficient C_1 ($= 1.0, 1.1, 1.15, 1.17$) in Eq. (17). With increasing C_1 , higher turbulence dissipation rates are expected. Simulation results are shown in Fig. 6b. As C_1 increases from the original default value (i.e. 1.0), the simulated TKE levels at the profiles of 3–5 gradually decrease and approach the measurements. Among these four simulations, the best fit is obtained for $C_1 = 1.15$. TKE at the profile locations 1, 2 and 6–8 are also reduced with a bigger C_1 . However, at the profiles of 9–11, the reverse tendency occurs, i.e. higher TKE is obtained for larger C_1 . This is understood from the resulting velocity profiles (Fig. 6c). As C_1 increases, the vertical velocity gradients at profiles of 9–11 increase strongly due to decreased vertical momentum diffusivity. This implies an increased TKE shear production rate (Eq. (17)) which explains the higher TKE at these locations.

Overall, an increased coefficient C_1 improves the model performance in terms of TKE in the breaking region. However, it also should be noted that this enlargement is not appropriate for all the locations in the surf zone. Apparently, similar to α_r , a cross-shore-varying rather than a constant value for C_1 seems more appropriate; the development of such a function could be a topic for further research. In addition, Fig 6c shows that the undertow magnitudes in the breaking region improve as C_1 increases, which implies that a proper description of the TKE can improve the mean flow results.

5.2. Obliquely incident waves on a natural, barred beach (DUCK' 94 experiment)

The developed model system is further evaluated by comparing model simulated wave-induced currents to measurements obtained on a natural sandy beach at Duck, North Carolina, during the DUCK94 experiment (e.g., Garcez Faria et al., 1998, 2000; U10; Kumar et al., 2011). Vertical profiles of velocities were obtained with a vertical stack of seven electromagnetic current meters (EMCs) located at elevations of 0.41, 0.68, 1.01, 1.46, 1.79, 2.24 and 2.57 m above the bed, and measured at seven surf zone cross-shore locations for approximately one hour at each site. Directional wave spectra were measured using 10 pressure sensors on an alongshore line at 8 m water depth (Long, 1996). Additionally, a spatially fixed cross-shore array of 11 EMCs and 13 pressure sensors were used to measure cross-shore variability of horizontal velocity and wave heights in the surf zone (Elgar et al., 1997). All data were collected on October 12 of 1994, when strong long-shore and cross-shore currents occurred due to waves generated by winds associated with the passage of a low pressure storm system. During data collection, the tidal variability was minimal and the bathymetric contours were assumed alongshore uniform (Garcez Faria et al., 2000). Further details on the data acquisition and processing can be found in Gallagher et al. (1996, 1998) and Elgar et al. (1997).

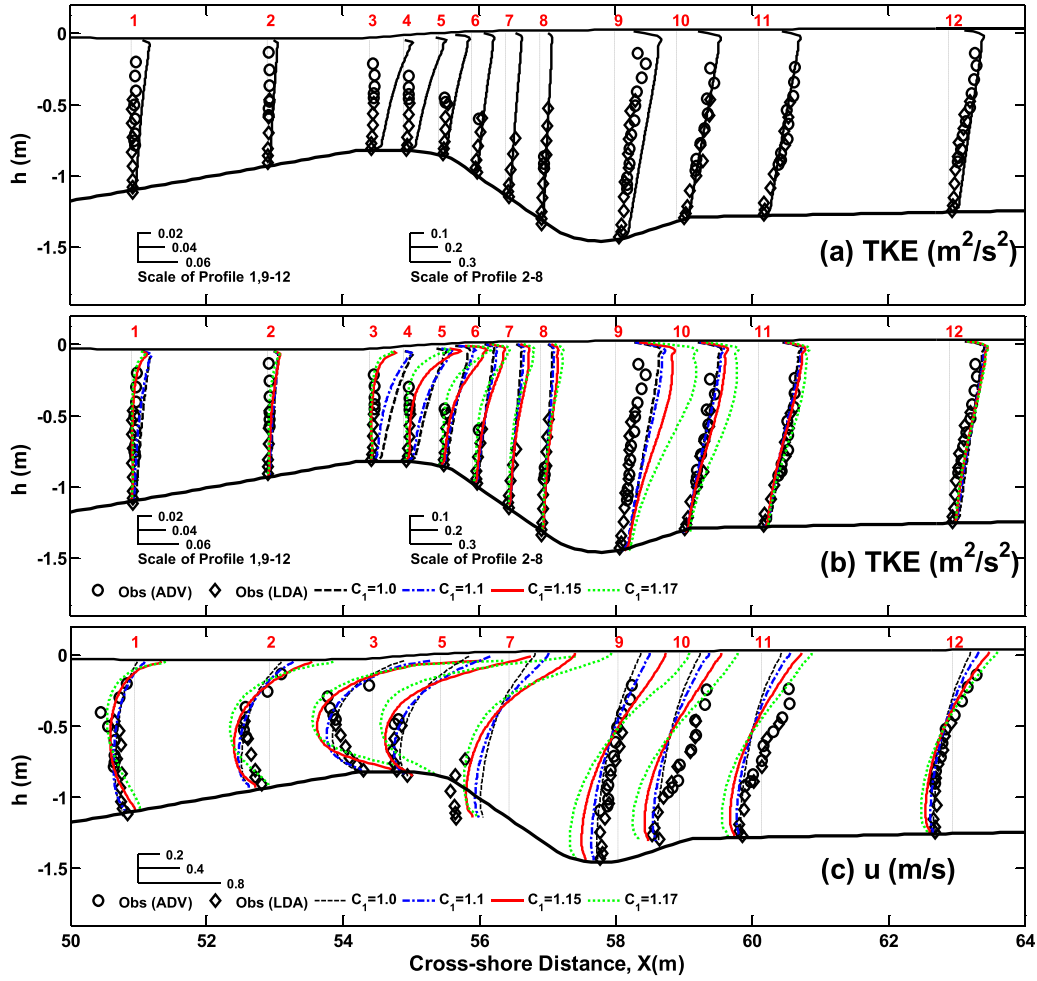


Fig. 6. Comparison of simulations (lines) with measurements (circles and diamonds) in terms of TKE (a, b) and time-averaged cross-shore velocities (c). (a) the standard run with $C_1 = 1.0$; (b) and (c) four simulations with $C_1 = 1.0, 1.1, 1.15, 1.17$. The vertical dashed lines indicate the profile measurement locations and zero value for each profile.

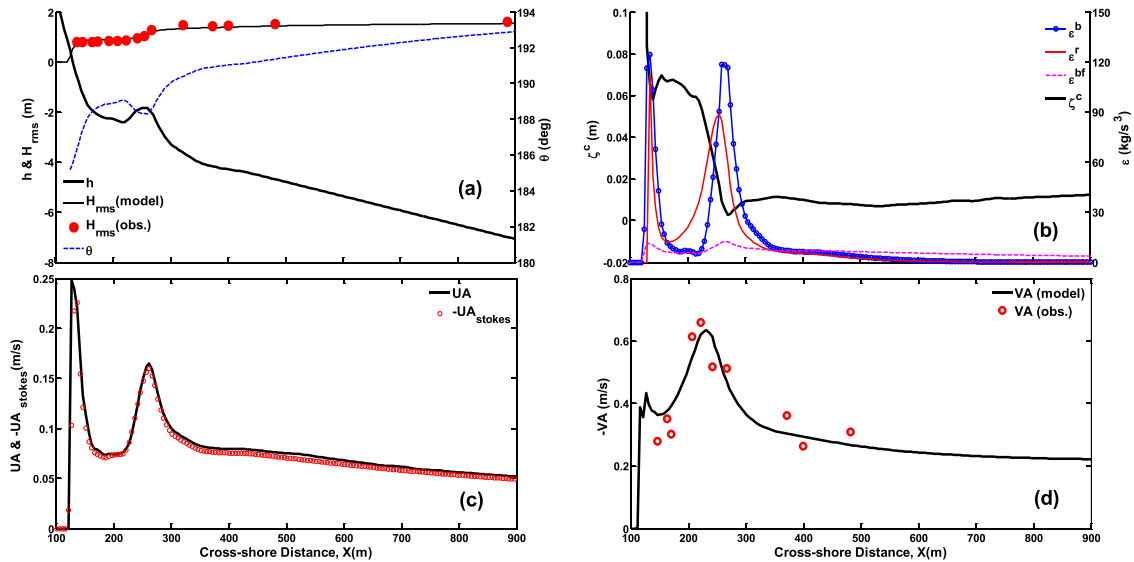


Fig. 7. Results of Duck94 simulation. Cross-shore distribution of: (a) root-mean-square wave height (H_{rms}) from model simulation (solid line) and observation (from Elgar et al., 1997; red circles), water depth (h) and simulated wave direction (θ); (b) sea surface elevation ζ^c , wave dissipation rates by depth-induced breaking ϵ^b , roller ϵ^r and bottom stress ϵ^{bf} ; (c) simulated depth-averaged cross-shore Eulerian velocity UA (solid line) and Stokes velocity $-UA_{stokes}$ (red circles); (d) depth-averaged Eulerian longshore velocity VA from simulation (solid line) and observation (from Feddersen et al., 1998; red circles). (For interpretation of the references to color in this figure legend, the reader is referred to the web version of this article).

Table 2
Model parameters for Duck94 simulation.

Variable	Value	Unit
Horizontal resolution	5	m
Time step	0.1	s
Offshore wave height H_{rms}	1.6	m
Offshore peak wave period T_p	6.0	s
Offshore incident wave angle θ_0	193.0°	
Roller dissipation parameter $\sin\beta$	0.1	
Offshore tidal elevation ζ_{tide}	0.7	m
Cross-shore wind stress $\tau_{sur}^{wind,x}$	-0.2532	N/m ²
Alongshore wind stress $\tau_{sur}^{wind,y}$	-0.1456	N/m ²
Coriolis frequency f	8.5695×10^{-5}	s ⁻¹
Lateral momentum diffusion coefficient Kh	0.1	m ² /s

The bathymetry used in the calculation is shown in Fig. 7a, with the shoreline located near $x = 120$ m and a nearshore bar located at about $x = 250$ m. With a horizontal resolution of 5 m in both x and y direction, the model domain is uniform alongshore and has a cross-shore (x) width of 800 m and an alongshore length (y) of 100 m with origin at $x = 100$ m and $y = 100$ m. The water depth varies from 2.5 m above the datum at the origin to 7.3 m at the off-shore boundary. A tidal elevation, assumed constant over the simulation period, of 0.70 m is added to the water level. In total 31 vertical sigma levels are used with grid-height refinement near the surface and bottom. A periodic boundary condition is imposed in the alongshore direction (i.e., north and south boundaries) and a wet/dry boundary condition is used at the shoreward boundary. At the offshore open boundary, the Flather radiation condition for the free surface (Flather, 1976) is adapted with nudging towards the quasi-static sea level $\hat{\zeta}$. The effect of earth rotation is included with a constant Coriolis frequency of 8.8695×10^{-5} /s. Wind stress forcing of -0.2532 and -0.1456 N/m² is imposed in the cross-shore and longshore directions, respectively. At the offshore boundary, a JONSWAP wave spectrum with a root-mean-square wave height of 1.6 m, a peak period of 6 s and a 13° angle of incidence is provided to the Un-SWAN model to obtain the wave field. The wave roller effect is also enabled with $\alpha_r = 1.0$, as sensitivity tests (not shown here) present overall best results with this value. However, as discussed in Section 5.1.2, this factor is more appropriate to be regarded as a function of the cross-shore positions. Instead of the β -kd parameterization, the constant breaker index ($\gamma = 0.73$) is used in this case to calculate the wave dissipation. Other model settings are the same as those used in Section 4.2. Note that the shoreline is located in the left side of the coordinate in this case, opposite to the former ideal and lab cases, thus $u > 0$ means velocity is offshore directed.

The model simulation is initiated with a resting state and carried out for a period of 6 h to obtain converged solutions with both baroclinic and barotropic time stepping of 0.1 s. The relevant model parameters are summarized in Table 2.

5.2.1. Wave parameters

Fig. 7a shows that the computed wave height H_{rms} that is in close agreement with the measured wave height (Elgar et al., 1997) throughout the beach profile. The wave direction, demonstrating clearly the effect of depth-induced refraction, turns from 193° at the offshore boundary to about 185° at the shoreline. The three dissipation terms calculated from the model (Fig. 7b) demonstrate that the depth-induced breaking (ε^b) occurs predominantly at the bar crest and at the nearshore region close to the shoreline. Over the bar trough, the wave dissipation is very small, which leads to the relatively stable wave height in this region (Fig. 7a). The roller dissipation (ε^r) peaks more shoreward than ε^b ; the bottom friction dissipation (ε^{bf}) is about one order of magnitude smaller than the other dissipation terms in the breaking region while it is dom-

inant at the offshore region ($x > 500$ m). The sea surface elevation (ζ^c) presents an overall trend of wave set-up outside and wave setup inside the surf zone (Fig. 7b), while around the breaking point a small decrease occurs due to the dominant contribution by the Bernoulli head (see details below), consistent with simulation results by U10 and K12. The depth-averaged Eulerian cross-shore velocity (Fig. 7c) is directed offshore and strongest over the bar crest and further shoreward. Similarly, to the plane beach test in Section 4.1, it also has the same magnitude but opposite sign to the depth-averaged Stokes flow, agreeing well with the barotropic mass conservation principle in alongshore-uniform, steady-state cases. The depth-averaged alongshore velocity (Fig. 7d) corresponds to the measurements (Feddersen et al., 1998) reasonably well, showing a general increase towards the shore with a peak value located over the bar trough and then a diminishing magnitude toward the shore.

5.2.2. Cross-shore and vertical structure of velocity

Fig. 8 presents the computed horizontal and vertical distribution of (\mathbf{V}, w) and $(\mathbf{V}^{St}, w^{St})$ in the x - z plane. Similar to the plane beach case, the distribution pattern of cross-shore velocity $u(x, z)$ shows an overturning circulation in the surf zone, with an onshore directed flow near the surface and offshore directed undertow near the bottom (Fig. 8a). This circulation cell has maximum strengths over the bar crest and close to the shoreline while being relatively weaker over the inner surf zone ($x = 150$ – 200 m). Outside the surf zone, currents are offshore directed and generally weak. In the lower layer of the water column the current reaches a maximum value which monotonically decrease to zero at the sea bed, while near the sea surface there is a small onshore directed contribution. In the horizontal x direction, the longshore velocity $v(x, z)$ (Fig. 8b) has a maximum negative value in the trough region shoreward of the bar. Vertically, the strongest longshore velocity occurs at the water surface and magnitudes decrease monotonically towards the sea bed.

The computed vertical velocity (Fig. 8c) shows upward directed velocities shoreward from the bar crest and downward directed velocities offshore from the bar-crest ($x = 250$ m), with maximum values located near the bottom. This pattern along with onshore flows near the surface and offshore directed undertow in the lower layers of the water column creates an anticlockwise circulation cell pattern over the bar trough inshore of the bar crest.

In accordance with the $\cosh(2kz)$ distribution suggested by Eq. (4), the 3D wave-induced cross-shore and longshore Stokes drift (u^{St}, v^{St}) are strongest near the surface and weakest near the sea bed, with maximum u^{St} and v^{St} above the bar crest and near the shoreline at shallow water (Fig. 8d and e). Due to the small obliqueness of the incident waves, v^{St} is almost an order of magnitude weaker than u^{St} . The distribution pattern of vertical Stokes velocity w^{St} is characterized by two pairs of upward and downward directed w^{St} dipole circulations, with the upward directed velocities located near the shoreline and shoreward from the bar crest, while downward directed velocities occurs offshore to these locations. The vertical Stokes velocity w^{St} is of the same magnitude as its Eulerian mean counterpart w , but has its maximum strength near the water surface. Additionally, Fig. 8d–f shows that the Stokes drifts have vertical variations even in water depth < 1 m, which confirms the presence of a vertically varying VF. As indicated by U10, the use of vertically varying VF in the model could lead to a simulation improvement compared to simulations (e.g. Newberger and Allen, 2007b) using vertically uniform VF.

A further model-data comparison is made for the cross-shore and longshore velocity at seven different surf zone locations in Fig. 9, which shows fairly good agreement between the simulated results and the observations. The normalized r.m.s. errors for u and v (as defined in Newberger and Allen, 2007b and U10) at a total of

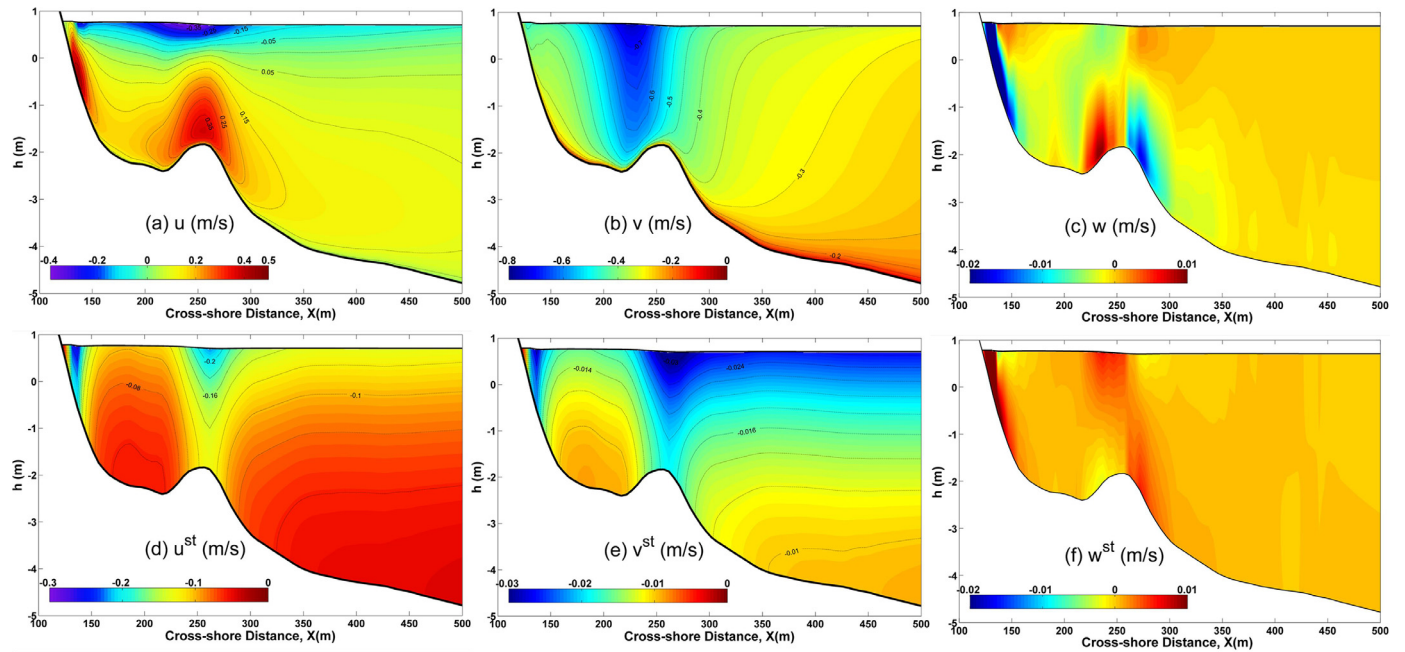


Fig. 8. Model simulated cross-shore distribution of (a) cross-shore velocity u ; (b) alongshore velocity v ; (c) vertical velocity w ; (d) cross-shore Stokes velocity u^{st} ; (e) alongshore Stokes velocity v^{st} ; and (f) vertical Stokes velocity w^{st} , for Duck94 experiment. Contour lines are used to show the velocity value explicitly.

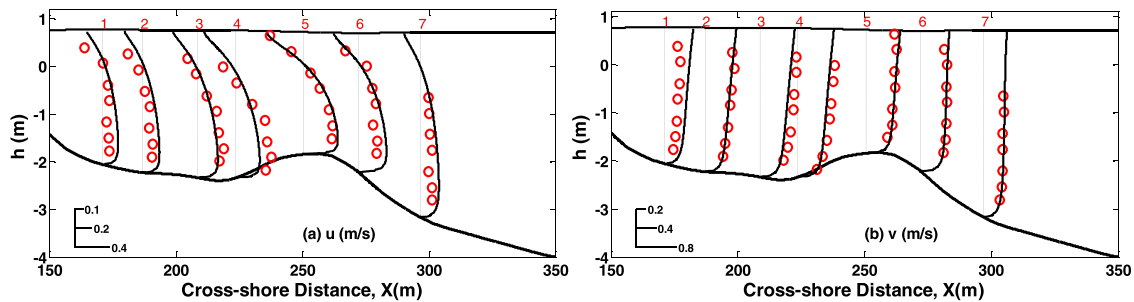


Fig. 9. Comparison of simulation results (solid lines) with observed vertical profiles (red circles) for cross-shore (a) and alongshore (b) velocities. The vertical dashed lines indicate the profile measurement locations and zero value for each profile (data from Garcez-Faria et al., 1998, 2000). (For interpretation of the references to colour in this figure legend, the reader is referred to the web version of this article).

Table 3

Normalized root mean square error $\epsilon_j = \left\{ \frac{\sum_{i=1}^{n_{stn}(j)} (d_{ij} - m_{ij})^2}{\sum_{i=1}^{n_{stn}(j)} (d_{ij})^2} \right\}^{1/2}$ for the cross-shore and longshore velocity estimates for Duck94 experiment for various locations across the profile. d_{ij} and m_{ij} represent measured (from Garcez-Faria et al., 1998, 2000) and model estimated velocity values at the 7 cross-shore locations (j) and various elevations (i) above the sea bed. Station 1 is closest to the shoreline.

STN #	mean	#1	#2	#3	#4	#5	#6	#7
Cross-shore	0.392	0.585	0.567	0.272	0.478	0.126	0.328	0.388
Longshore	0.120	0.416	0.043	0.131	0.092	0.039	0.075	0.043

42 measurement positions are summarized in Table 3. The mean r.m.s. errors at 7 locations are 0.39 for u and 0.12 for v , which is similar to those shown by U10 (u error and v error range 0.45–0.70 and 0.10–0.40, respectively) and slightly better than those in K12 (u error and v error range 0.54–0.66 and 0.21–0.30, respectively). These simulated results show that the developed model system in this study is capable of creating realistic velocity profiles in a surf zone environment.

Similar to the laboratory breaking wave test case in Fig. 5b, the computed cross-shore velocity magnitudes at the shoreward side of the breaker bar (the 3rd and 4th profiles) are significantly underestimated. Eight sensitivity simulations with a variation of the turbulent coefficient C_1 are firstly conducted, which is inspired by

the analysis in Section 5.1.3, as a preliminary attempt to reveal the effect of turbulence on the cross-shore velocities and to improve the simulation results. Table 4 summarizes the normalized r.m.s. errors of these simulations. Apparently, a sole value of C_1 (run 1–8) cannot decrease the normalized r.m.s. error at all cross-shore locations simultaneously. It is found that C_1 has a best fit value of 1.10 for the 3rd and 4th profiles and 0.85 for the 5th profile; while in the remaining 4 profiles, 0.80 is optimum. This is in agreement with the results in Section 5.1.3, which also suggested a locally higher C_1 value for the breaking region around the bar crest. Based on the simulation results of Runs 1–8, another simulation (Run 9) was conducted with cross-shore-varying C_1 , i.e. $C_1 = 1.10$ at cross-shore locations between the 3rd and 4th profiles

Table 4
Normalized root mean square error analysis for cross-shore velocity with different values of C_1 .

RUN#	STN #								Mean	C_1
	#1	#2	#3	#4	#5	#6	#7			
1	0.515	0.565	0.615	0.871	0.082	0.238	0.303	0.456	0.80	
2	0.529	0.562	0.546	0.792	0.073	0.256	0.319	0.440	0.85	
3	0.544	0.560	0.468	0.703	0.076	0.276	0.337	0.423	0.90	
4	0.562	0.561	0.378	0.601	0.094	0.299	0.360	0.408	0.95	
5	0.585	0.567	0.272	0.478	0.126	0.328	0.388	0.392	1.00	
6	0.609	0.579	0.154	0.334	0.170	0.364	0.420	0.376	1.05	
7	0.640	0.598	0.131	0.166	0.220	0.403	0.467	0.375	1.10	
8	0.674	0.634	0.351	0.181	0.275	0.457	0.531	0.443	1.15	
9	0.506	0.560	0.135	0.215	0.080	0.238	0.303	0.291	*	

* $C_1 = 1.10$ at cross-shore locations between the 3rd and 4th profiles and 0.80 at the remainder locations.

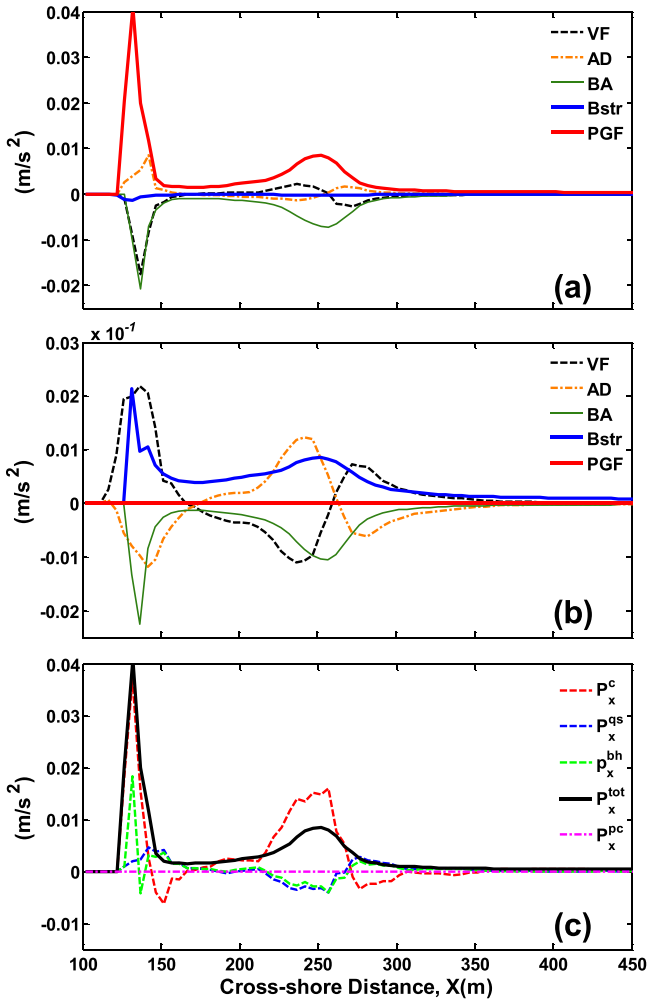


Fig. 10. Cross-shore profiles of depth-averaged (a) cross-shore and (b) longshore momentum balance terms; (c) decomposed PGF terms in cross-shore direction as described in Eq. (23).

and $C_1 = 0.80$ at the remainder of the locations, leading to much better results (Table 4).

5.2.3. Horizontal momentum balance

In order to understand the mechanisms responsible for these 3D model results, similar to the descriptions of Section 4.7 in U10, the cross-shore depth-averaged and vertical variation of momentum balances are analysed and displayed in Fig. 10 and Fig. 11 respectively. Table 5 summarizes the physical meanings of relevant

symbols used in the following text for representing the momentum balances.

The two-dimensional momentum balance in the cross-shore direction (Fig. 10a) demonstrates a primary balance between the pressure gradient (P^{tot}) and the breaking acceleration (BA) term. This is consistent with the classic surf-zone momentum balance between wave-setup and breaking acceleration (cf., Bowen et al., 1968). A secondary balance also exists between the advection and the VF terms as these two terms have similar magnitude but opposite sign at all cross-shore locations. Fig. 10a also shows that these four terms are only relatively strong near the bar-crest and near the shoreline, but are negligibly small elsewhere. Similar to the balance in cross-shore direction, the alongshore momentum also demonstrates two sets of balances: a primary balance between the breaking acceleration and the bottom stress terms and a secondary one between the advection and vortex force terms. The existence of these secondary balances in cross-shore and longshore momentum are actually required by the barotropic mass balance (Uchiyama et al., 2009) which results in the anti-Stokes u flow for an alongshore-uniform, steady circulation (Fig. 7c for this case and Fig. 1c for plane beach case). However, it is important to point out that although the alongshore vortex force generally opposes alongshore advection at most of the cross-shore locations, due to differences in vertical structure of Stokes and Eulerian mean flows these two terms do not cancel out completely.

The contribution of the pressure gradient force is investigated in more detail. For this, the total pressure gradient force, P^{tot} (i.e. $\nabla\phi$, taken from Eq. (B13) by excluding the vertical vortex force term K from $\nabla\phi^c$), is firstly decomposed into two terms which respectively describe the contribution from the non-WEC (P^c) and WEC (P^{wec}) terms. P^{wec} is further decomposed into a quasi-static response P^{qs} , a Bernoulli head contribution P^{bh} and a WEC surface pressure boundary correction P^{pc} term:

$$\begin{aligned}
 P^{tot} &= P^c + P^{wec} = P^c + (P^{qs} + P^{bh} + P^{pc}) \\
 &= -\nabla_{\perp} \left(g\zeta^c + \int_{-h}^z \frac{g\rho}{\rho_0} dz \right) + (g\nabla_{\perp} \hat{\zeta} + \nabla_{\perp} \mathcal{K}|_{\zeta^c} + \nabla_{\perp} \mathcal{P}|_{\zeta^c})
 \end{aligned}
 \tag{23}$$

Analysis of these individual components of the total pressure gradient force P_x^{tot} Fig. 10c shows that, except for the surface pressure boundary correction term (P_x^{pc}), in the surf zone all the other three terms (i.e. P_x^c , P_x^{bh} and P_x^{qs}) have significant contributions to P_x^{tot} , with the non-WEC response term P_x^c contributing most. Outside the surf zone, however, all these terms become very small. It is important to note that in the region between the trough and crest of the bar, where high velocity shear contributes significantly to P_x^{bh} , the contribution by P_x^{bh} modifies P_x^{tot} significantly and the term thus plays an important role in this region. This is an improvement to the classical view of the barotropic cross-shore momentum balance (cf., Bowen et al., 1968; Uchiyama et al., 2009) which suggests that P_x^{tot} is primarily controlled by P_x^c and P_x^{qs} . As suggested by U10, this is also the major factor that causes the difference in the wave-induced sea-level setup between the 2D (not shown here) and 3D cases.

The vertical variation of the momentum balances is shown in Fig. 11. In the cross-shore direction, the breaking acceleration (x-BA, Fig. 11a), pressure gradient (x-PGF, Fig. 11d) and vertical mixing (x-VM, Fig. 11e) terms are the major contributors to the momentum balance with strongest values occurring at locations where total wave dissipation is maximum, while the advection (x-AD, Fig. 11b) and vortex force (VF, Fig. 11c) terms are relatively weak and insignificant. Note that the VF term here is dominated by the vertical VF contribution. In this 3D cross-shore momentum balance, the VM term apparently plays an important role. It vertically trans-

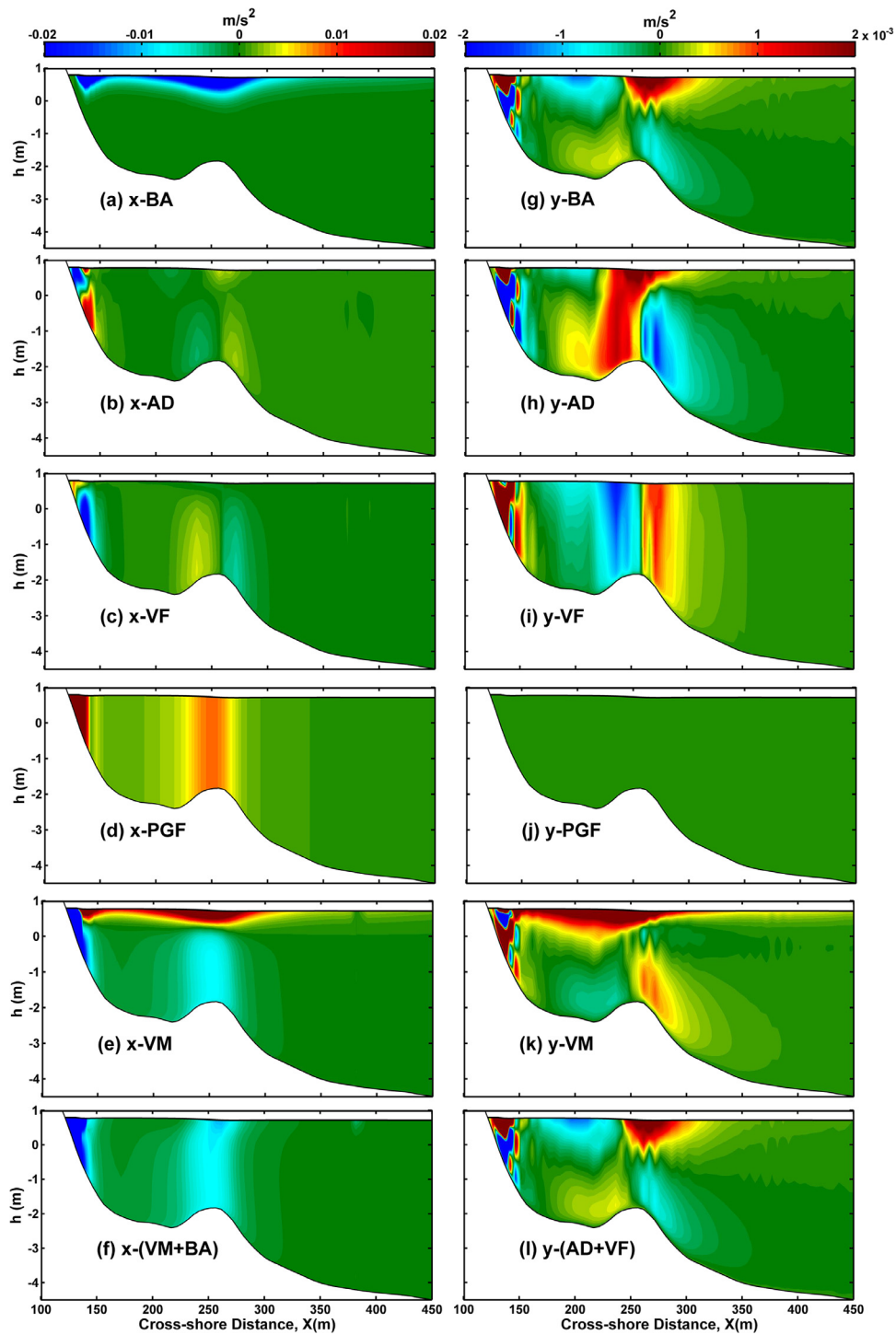


Fig. 11. Cross-shore and vertical distribution of the terms contributing to the cross-shore (x) and longshore (y) momentum balance. Cross-shore terms: (a) x-breaking acceleration (x-BA); (b) x-Eulerian advection (x-AD); (c) x-vortex force (x-VF); (d) x-pressure gradient force (x-PGF); (e) x-vertical mixing (VM); (f) x-vertical mixing plus breaking acceleration (x-VM+BA); and alongshore terms: (g) y-breaking acceleration (y-BA); (h) y-Eulerian advection (y-AD); (i) y-vortex force (y-VF); (j) y-pressure gradient force (y-PGF); (k) y-vertical mixing (y-VM); and (l) y- advection plus vortex force (y-AD+VF).

fers the surface-intensified BA down to the bottom (Fig. 11f) with a near vertically-uniform distribution, and consequently it balances the nearly barotropic pressure gradient force (x-PGF, Fig. 11d).

In the longshore direction, all the remaining terms (i.e., y-BA, y-AD, y-VF and y-VM) with the exception of y-PGF demonstrate significant contributions to the 3D momentum balance, in which the sum of y-BA and y-AD are balanced by the sum of y-VF and y-VM. The breaking acceleration y-BA displays a similar distribution to x-

BA but is one order of magnitude smaller due to the small obliqueness of the incident waves. All of the terms of y-AD, y-VF and y-VM demonstrate evident 3D structures which implies that it is necessary to have a fully 3D structure for the Stokes drift and VF even in shallow littoral regions like DUCK94. Similar to the longshore depth-averaged balance where vortex force balances advection, the y-VF and y-AD also seems to balance each other in this 3D budget. However, they do not completely cancel each other (Fig. 11l), but

Table 5
List of symbols used for representing the momentum balances.

Individual terms	Description	Expression
BA	Breaking acceleration induced by wave breaking and roller	$F_x^w = \frac{e^{wcap} + (1 - \alpha_c)e^{\epsilon} + \epsilon^2}{\rho_0 \sigma} \mathbf{k} \cdot \mathbf{f}^b(z)$
AD	Advection term	$-\frac{1}{D} \left(\frac{\partial u^2 D}{\partial x} + \frac{\partial uv D}{\partial y} + \frac{\partial uv^2}{\partial s} \right)$
VF	Vortex Force term	$v^{st} \left(\frac{\partial v}{\partial x} - \frac{\partial u}{\partial y} \right) - \frac{u}{D} \left(\frac{\partial u^2 D}{\partial x} + \frac{\partial uv^2}{\partial y} \right)$
VM	Vertical Mixing	$+\frac{\partial}{\partial x} \left[\int_s^0 \left(u^{st} \frac{\partial u}{\partial \sigma} + v^{st} \frac{\partial v}{\partial \sigma} \right) ds \right]$
PGF/ P^{tot}	Total pressure gradient force	$\frac{\partial}{\partial s} \left(\frac{K_M}{D^2} \frac{\partial u}{\partial s} + \frac{v}{D^2} \frac{\partial u}{\partial s} \right)$
P^c	Non-WEC current contribution	$-\frac{\partial \phi^c}{\partial x} = -\frac{\partial}{\partial x} \{ g(\zeta^c - \hat{\zeta}) - (P _{\zeta^c} - \mathcal{K} _{\zeta^c}) + \int_s^0 \frac{g\rho D}{\rho_0} ds \}$
P^{wec}	WEC contribution	$-\frac{\partial}{\partial x} \left(g\zeta^c + \int_s^0 \frac{g\rho D}{\rho_0} ds \right)$
P^{qs}	Quasi-static response	$\mathbf{P}^{qs} + \mathbf{P}^{bh} + \mathbf{P}^{pc}$
P^{bh}	Bernoulli head	$g \frac{\partial \zeta}{\partial x}$
P^{pc}	Surface pressure boundary correction	$-\frac{\partial}{\partial x} (\mathcal{K} _{\zeta^c})$

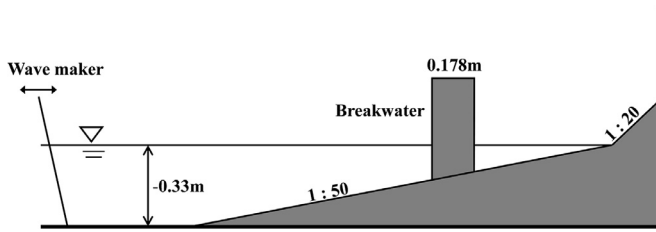


Fig. 12. Experimental layout of Hamm et al. 1995.

instead, their sum yields a net contribution that modifies the flow pattern.

5.3. Normally incident waves on a plane beach with shore-parallel breakwater

To further demonstrate the flexibility of the unstructured mesh in the present model, the laboratory experiment of Hamm et al. (1995) was numerically simulated. The experiment involved regular waves propagating and breaking around a shore-parallel breakwater on a plane beach in a large scale wave tank at Sogreah Ingenierie. The layout of the plane beach with the breakwater is presented in Fig. 12. In this test case, wave diffraction behind the breakwater induces complex three-dimensional flow patterns. The model is used to simulate the REG0107 test, which comprised detailed measurements of wave height and flow velocity (undertow) profiles at various positions around the breakwater. Fig. 13a shows the model domain (a cross-shore width of 26 m and an alongshore length of 60 m), measurement locations and the position of the breakwater of 6.66 m long and 0.90 m wide placed 9.3 m from the shoreline. The triangular mesh grid used in this case are shown in Fig 13b, in which the mesh is locally refined behind the breakwater (with a resolution of about 0.22 m) in order to obtain comparatively high resolution results there. However, given the rather simple geometry of this case, the simulation can only be regarded as a preliminary and limited demonstration of the flexibility of the unstructured mesh, which has more added benefit for cases with a much more complicated coastline. The model settings are the same as for the ideal plane beach case (Section 4), except that the wave information at the offshore boundary is provided by normally incident regular waves with wave height of 0.78 m and wave period of 1.69 s and no flow boundary conditions are utilized at the shoreline and lateral ends. The built-in feature 'OBSTACLE' of the Un-SWAN is utilized to simulate the wave diffraction around the breakwater with a constant transmission coefficient of 0.3 to mimic the structure porosity. The wave diffraction is approximated with a phase-decoupled refraction–diffraction approach proposed by Holthuijsen et al. (2003), which however has some limitations

(N. Booij, et al., 2015). The simulation is conducted for 1 h before the solution converged, with a barotropic time step of 0.05 s and a mode-splitting ration of 6.

Fig. 14 shows the distribution of computed wave height and depth-averaged flow velocity for this case. The wave diffraction as well as two large flow circulations can be seen clearly behind the breakwater. These two circulations are symmetric as the wave propagates with normal incidence to the shoreline, corresponding well with the results of Li et al. (2007). Fig. 15 shows the measured and computed wave heights, and alongshore and cross-shore depth-averaged velocity distributions along several along-shore transects behind the breakwater. As the waves propagate perpendicular to the shoreline, the computed wave height and wave induced cross-shore velocity are symmetrical along the centre of the breakwater (i.e. $X = 30$ m), while the wave-induced alongshore velocity has the same magnitude but opposite sign for each side of the $X = 30$ m axis. Compared with the measurements, the model predicted wave heights are fairly good along the major part of the selected four transects. However, in the places close to the tip of the breakwater (around $X = 40$ m) in the transect 2 and 3, the simulated wave height is under-predicted which is largely attributed to reflection processes which are not properly resolved by the wave model for this case. The predicted longshore and cross-shore velocity are also found to be fairly close to the measurements in all regions, apart from the under-predicted cross-shore velocities around $X = 40$ m due to the under-predicted wave height there.

The predicted long-shore and cross-shore velocity vertical profiles are further compared with the laboratory data at several points (points A–I in Fig. 13a) around the breakwater; details are shown in Fig. 16. Similar to the depth-averaged velocities in Fig. 15, the predicted long-shore velocity profiles agree well with the measurements at almost all positions, except for position F where the predicted profile has the correct magnitude but is of opposite sign compared to the laboratory data. This is attributed to the poorly-predicted depth-averaged longshore velocity shown at $X = 10$ m in Fig. 15g. The predicted cross-shore velocity profiles are also fairly good compared with measurements at most positions. The differences between the computed and measured cross-shore velocities are largely due to the discrepancies involved in the depth-averaged cross-shore velocity as shown in Fig. 15, which in return arise because of discrepancies in the wave height. Another explanation for the discrepancies in the cross-shore velocity is the highly non-uniform flow for this experiment, which induces strong horizontal gradients and relatively large discrepancies between measured and modeled cross-shore velocities for relatively small offsets in the predicted location of the circulations (as also indicated by Rakha, 1998).

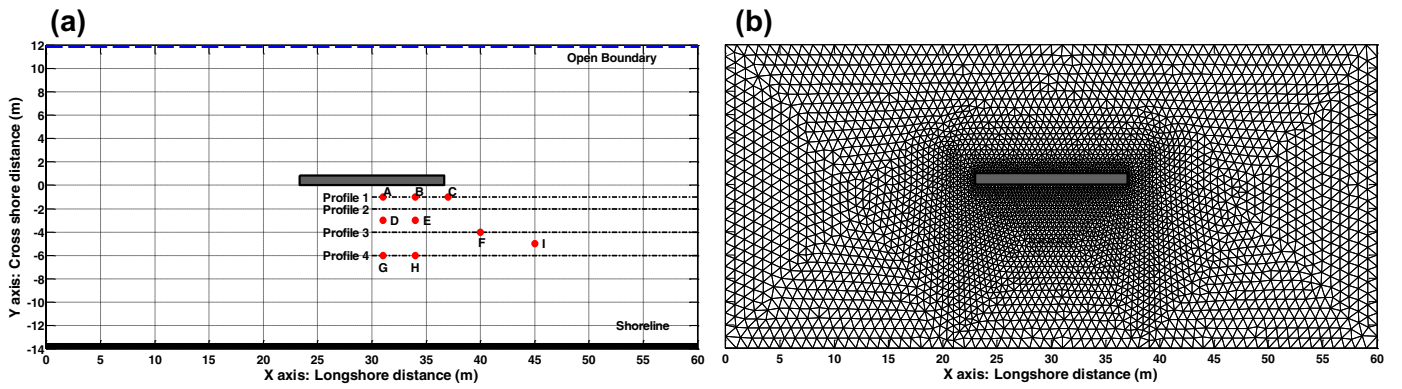


Fig. 13. (a) Model domain and measurement profiles and points of Hamm et al. (1995), the open boundary is located at $Y = 12$ m; (b) the horizontal unstructured triangular grids used for the simulations of the breakwater case.

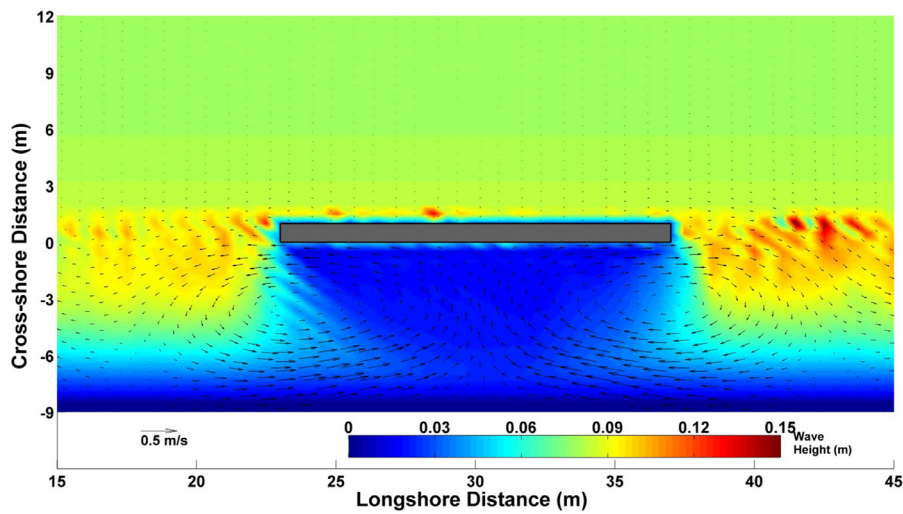


Fig. 14. The wave height (colour) and depth-averaged velocity (vector).

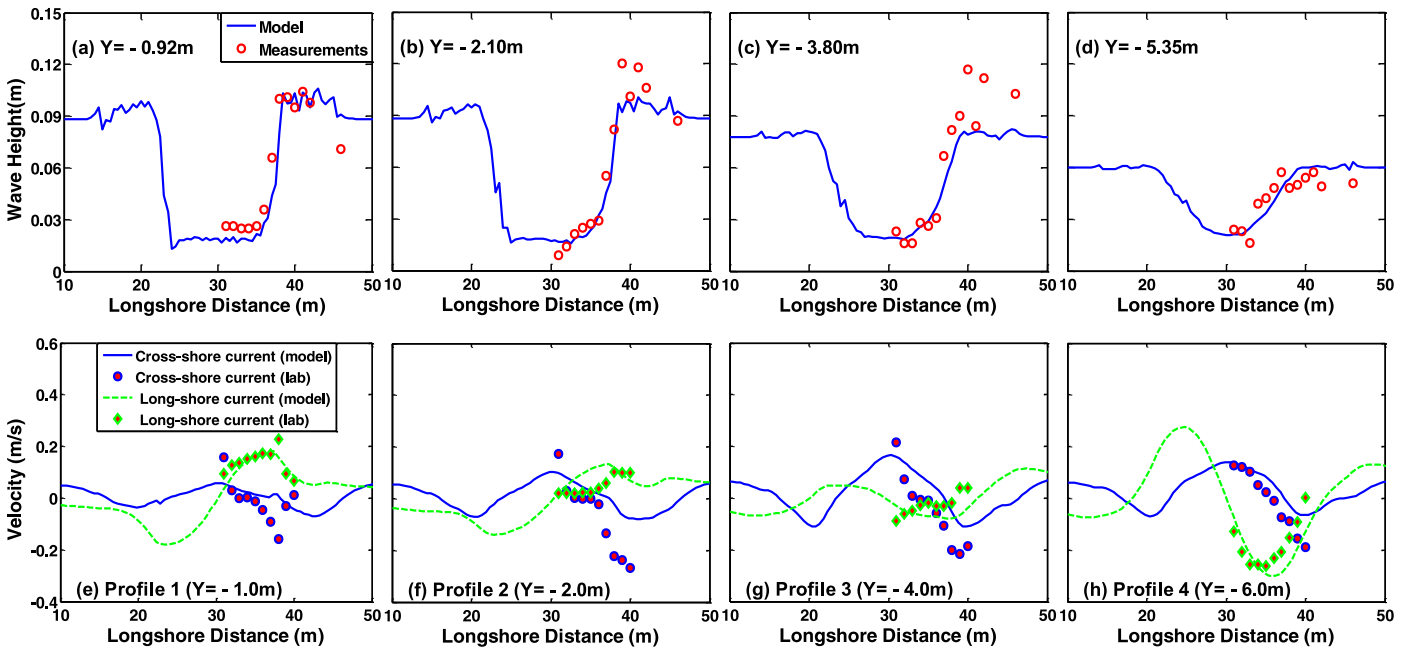


Fig. 15. Comparison of model predicted and measured wave height (a–d), alongshore and cross-shore velocity distribution (e–h) along a number of transects in the Hamm et al. (1995) experiment, test REG0107.

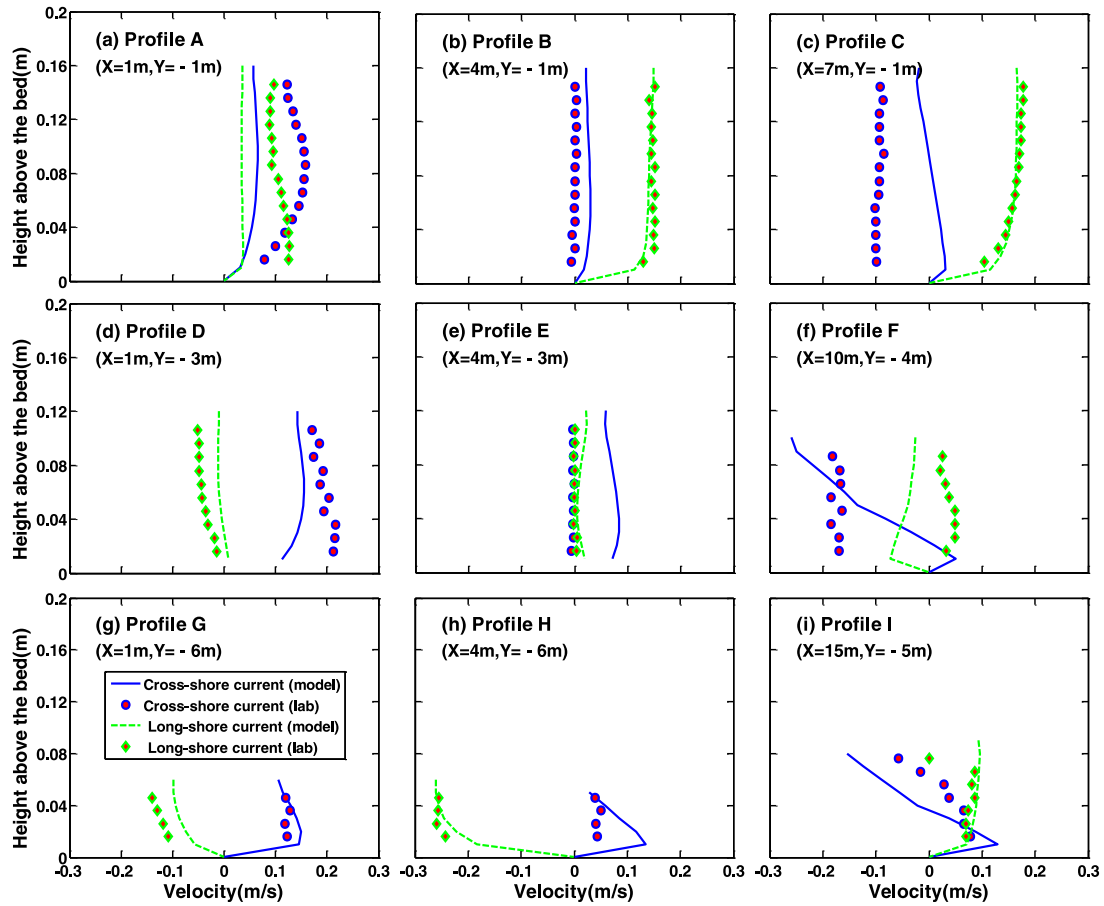


Fig. 16. Comparison of model predicted and measured velocity vertical profiles at a number of positions in the Hamm et al. (1995) experiment, test REG0107.

Overall, the present simulation conducted by the new model system in this study successfully reproduces the complex flow structures involving a wave-induced current interacting with a shore-parallel breakwater. There are some discrepancies involved in the velocity profiles due to the under-prediction of wave height resulting from the limited performance of the wave diffraction simulation in the wave model. A better prediction of the wave statistics would likely lead to a better prediction of the flow pattern. However, the overall qualitatively good representation of the dominant flow structures suggests the implementation of the wave-current interaction based on the VF approach is appropriate.

6. Conclusions

A new three-dimensional hydrodynamic model has been developed in the present study by coupling the third generation spectral wave model SWAN with the oceanographic model FVCOM. The vortex-force (VF) formalism is implemented to represent wave-current interactions. A new wave-current coupling scheme is developed, including a GLS turbulence model to reproduce the wave-breaking enhanced turbulence, as well as a roller transport model to account for wave breaking under influence of the surface roller. By adapting the unstructured grid version of SWAN (Un-SWAN), this new approach is novel in both numerical and practical aspects: the numerical procedure remains stable for any time step, and is locally implicit and globally explicit without requiring too much computational work as do implicit methods (Zijlema, 2010; N. Booij et al., 2015); the Un-SWAN utilizes the same triangular grids as FVCOM which circumvents the interpolation between different sets of computation grids.

This modeling system was firstly validated against a theoretical case of obliquely incident waves on a planar beach. It was then applied to three test cases for both validation and dynamical interpretation: a large scale laboratory experiment of normally incident waves on a rigidized barred beach, a field experiment of obliquely incident waves on a natural sandy barred beach (Duck' 94 experiment), and a 3D laboratory experiment involving normal incident waves propagating around a shore-parallel breakwater. The model predictions follow the available measurements in these tests well, suggesting robustness and efficiency in the present model for very different spatial scales and for both 2D and 3D complex hydrodynamic conditions. A general encountered difficulty in many coastal hydrodynamic simulations under breaking waves is the reproduction of Eulerian and Stokes velocities across the beach. The model results for the above applications suggest that the VF approach is capable of reproducing these balanced flow patterns for various types of beach and wave conditions.

Model simulations of the Duck 94 experiment indicate clearly that the VF is important in determining the two levels of momentum balance in both cross-shore and longshore flows. The VF method also represents the complex 3D wave dynamics and wave-driven circulation patterns around a laboratory breakwater. The simulation of the laboratory breaking wave over a barred beach indicates the importance of roller effects and of wave energy dissipation on the cross-shore mean flow (undertow) profiles. In this particular case, the empirical parameter α in Eq. (A7) with a value of 0.75 produces the best fit with the measured data. Different values were tested for α_r (fraction of wave energy dissipation converted to roller) and for the C1 parameter that controls turbulent dissipation rates; results suggest that both parameters should vary across

the breaking region for a better model accuracy. A better reproduction of the turbulent kinetic energy also leads to an improved reproduction of the undertow velocity profile.

Overall the newly developed modeling system with implementation of VF formalism successfully resolves waves and currents in the surf zone. The modeling system provides a robust tool for better understanding of hydrodynamic processes in coastal regions, and may in the future also be used to explore sediment transport processes and morphodynamics in coastal regions.

Acknowledgments

This work was partly supported by joint Engineering and Physical Science Research Council (EPSRC) UK and Technology Foundation STW Netherlands funded SINBAD (EP/J005541/1) project. P. Zheng was supported by the China Scholarship Council during his four-year PhD study at the University of Liverpool. We would like to thank Prof. C.S. Chen of the University of Massachusetts-Dartmouth for providing the source code of FVCOM and also the SWAN developers for developing and providing this open source code. We would also like to thank the staff and personnel involved in collecting and maintaining the DUCK'94 experiment dataset and the anonymous reviewers for their constructive comments and suggestions. Computational support was provided by the Chadwick High Performance Computer at University of Liverpool and also the facilities of N8 HPC Centre of Excellence, provided and funded by the N8 consortium and EPSRC (EP/K000225/1).

Appendix A. Parameterization of non-conservative wave acceleration

A1. Acceleration induced by whitecapping (\mathbf{B}^{wcap})

White-capping is controlled by the wave steepness. In Un-SWAN, many different expressions for white-capping have been formulated, e.g. the pulse-based model (Hasselmann, 1974) that is commonly used in the third-generation operating wave model, and a saturation-based model (Alves and Banner, 2003; Van der Westhuysen et al., 2007). Taking the value of white-capping dissipation (ε^{wcap}) calculated in Un-SWAN, the associated acceleration could be expressed either as a body force,

$$\mathbf{B}^{wcap} = \frac{\varepsilon^{wcap}}{\rho_0 \sigma} \mathbf{k} \cdot f^b(z) \quad (A1)$$

or as a boundary stress,

$$\tau_{sur}^{wcap} = \rho_0 D \bar{\mathbf{B}}^{wcap} = \frac{\varepsilon^{wcap}}{\sigma} \mathbf{k} \quad (A2)$$

where $f^b(z)$ is an empirical vertical distribution function that quantifies the vertical penetration of momentum associated with breaking waves from the surface, given by

$$f^b(z) = \frac{\cosh[k_b(h+z)]}{\int_{-h}^{\zeta_c} \cosh[k_b(h+z)] dz} \quad (A3)$$

where $k_b^{-1} = a_b H_*$ is a decay parameter that controls the penetration depth; H_* is square mean wave height; a_b is an empirical constant that is set to 0.2 in this study.

A2. Depth-induced breaking (ε^b) and acceleration (\mathbf{B}^{db})

In Un-SWAN, the bore model of Battjes and Janssen (1978) is used to compute the depth-induced breaking (ε^b), given by

$$\varepsilon^b = -\frac{\rho g}{4} \alpha_{BJ} Q_b \tilde{f} H_{max}^2 \quad (A4)$$

where $\alpha_{BJ}=O(1)$ is a tunable coefficient; Q_b is the fraction of breaking waves; \tilde{f} is the mean wave frequency; and H_{max} is the

maximum possible wave height at local water depth d , controlled by $H_{max} = \gamma d$ where γ is an adjustable breaking coefficient. In this study, γ is either given as a constant value (0.73) or determined by a recently proposed β -kd parameterization (Salmon et al., 2015).

The depth-induced wave breaking acceleration (\mathbf{B}^{db}), as a body force, is provided by,

$$\mathbf{B}^{db} = \frac{(1 - \alpha_r) \varepsilon^b}{\rho_0 \sigma} \mathbf{k} \cdot f^b(z) \quad (A5)$$

where α_r is the fraction of wave dissipation converted into rollers (described in details later); $f^b(z)$ is an empirical vertical distribution function, which utilizes the same function as defined in Eq. (A3).

The depth-induced wave breaking acceleration (\mathbf{B}^{db}) is alternatively incorporated into the momentum equation as an equivalent boundary stress,

$$\tau_{sur}^b = \rho_0 D \bar{\mathbf{B}}^{db} = \frac{(1 - \alpha_r) \varepsilon^b}{\sigma} \mathbf{k} \quad (A6)$$

A3. Wave rollers and acceleration induced by rollers (\mathbf{B}^r)

Within the surf zone, where the bathymetry-dependent breaking of waves is the dominant factor in the spatial distribution of wave energy dissipation, the action of wave rollers also play an important role in this process. Surface wave rollers are onshore-traveling bores of broken primary waves which store the dissipated wave energy and transfer it gradually into the mean flow, causing a lag in the transfer of momentum (Svendsen, 1984; Nairn et al., 1991). The surface wave rollers are included in the present fully coupled wave-current interaction system to improve calculations of the surf zone currents.

The surface roller model in the present study is based on existing approaches of Stive and De Vriend (1994) and Reniers et al. (2004a). Analogous to the spectral wave evolution equation, the evolution equation for the wave roller energy is represented as:

$$\frac{\partial E^r}{\partial t} + \frac{\partial}{\partial x} (C_x E^r) + \frac{\partial}{\partial y} (C_y E^r) = \alpha_r \varepsilon^b - \varepsilon^r \quad (A7)$$

where E^r is the surface roller energy; $\mathbf{C} (C_x, C_y)$ is the phase speed of the primary wave, given by $\bar{\mathbf{V}} + \frac{\sigma}{k} \frac{\mathbf{k}}{k}$; ε^b is the dissipation of wave energy which is a source term for the roller energy; ε^r is the roller energy dissipation rate; α_r is an *ad hoc* empirical parameter introduced by Tajima and Madsen (2006), denoting the fraction of wave dissipation feeding the wave roller (value between 0 and 1). As suggested by U10, α_r provides some flexibility to depict different beach forms and wave breaking types (i.e. spilling, plunging, surging). The roller dissipation rate can be parameterized by $\varepsilon^r = \frac{g \sin \beta E^r}{c}$, where c is the phase speed and $\sin \beta (=0.1)$ is an empirical constant (Reniers et al., 2004a).

The acceleration induced by wave rollers is given as, in the form of a body force,

$$\mathbf{B}^r = \frac{\varepsilon^r}{\rho_0 \sigma} \mathbf{k} \cdot f^b(z) \quad (A8)$$

and in the form of a boundary stress,

$$\tau_{sur}^r = \rho_0 D \bar{\mathbf{B}}^r = \frac{\varepsilon^r}{\sigma} \mathbf{k} \quad (A9)$$

Combining Eqs. (A1), (A5) and (A8), the total force induced by surface wave breaking (i.e. white-capping, depth-induced wave breaking and surface wave rollers) reads

$$\mathbf{B}^{swb} = \frac{\varepsilon^{wcap} + (1 - \alpha_r) \varepsilon^b + \varepsilon^r}{\rho_0 \sigma} \mathbf{k} \cdot f^b(z) \quad (A10)$$

and the corresponding boundary stress reads

$$\tau_{sur}^{swb} = \rho_0 D \bar{\mathbf{B}}^r = \frac{\varepsilon^{wcap} + (1 - \alpha_r) \varepsilon^b + \varepsilon^r}{\sigma} \mathbf{k} \quad (A11)$$

This boundary stress could be taken as an augmentation to the usual oceanic-model representation of surface wind stress (τ_{sur}^{wind}), which at the same time the momentum flux from atmosphere to wave (τ_{sur}^{wave}) need to be subtracted. Hence, the total surface stress becomes

$$\tau_{sur} = \tau_{sur}^{wind} + \tau_{sur}^{swb} - \tau_{sur}^{wave} \quad (A12)$$

Wave rollers also contribute to the Stokes transport. Following Svendsen (1984), the roller Stokes transport is given by

$$\mathbf{U}^r = \frac{E^r}{\rho_0 \sigma} \mathbf{k} \quad (A13)$$

Thus the total Stokes transport becomes

$$\mathbf{U}^{st} = \frac{(E + E^r)}{\rho_0 \sigma} \mathbf{k} \quad (A14)$$

If the same vertically distribution of the Stokes drift velocity (Eq. (4)) is assumed for the vertical profile of \mathbf{U}^r , the total Stokes drift velocity reads

$$\mathbf{V}^{st} = \frac{\cosh[2Z]}{\sinh[2H]} \frac{2(E + E^r)}{c} \mathbf{k} \quad (A15)$$

As suggested by U10 and K12, a surface-intensified vertical structure (e.g. Haas and Warner, 2009; hereinafter named HW09) may be more suitable for \mathbf{U}^r . However, the simulation results using these two vertical distributions are very similar (K12). Hence, for simplicity, the Stokes velocity type of distribution is used in this study.

A4. Bottom friction dissipation (ε^{bf}) and accelerations due to bottom streaming (\mathbf{B}^{bf})

The surface-wave-induced orbital motions extend down to the sea floor in shallow water, causing interactions between the surface waves and the bottom. In these wave-bottom interactions, the bottom friction is a dominant wave dissipation mechanism for continental shelf seas with sandy bottoms (Bertotti and Cavaleri, 1994). Following Reniers et al. (2004b), the bottom friction induced wave dissipation (ε^{bf}) is parameterized by

$$\varepsilon^{bf} = \frac{1}{2\sqrt{\pi}} \rho_0 f_w |u_{orb}^w|^3 \quad (A16)$$

where $|u_{orb}^w| = \frac{\sigma H_s}{2\sqrt{2} \sinh kD}$ is the wave bottom orbital velocity and $f_w = 1.39 \left(\frac{\sigma z_b}{|u_{orb}^w|}\right)^{0.52}$ is the wave friction factor (Soulsby, 1995).

Dissipation of wave energy in the wave boundary layer causes the instantaneous, oscillatory wave bottom orbital velocities to be not exactly ninety degrees out of phase, resulting in a wave stress (bottom streaming) in the wave bottom boundary layer along the direction of wave propagation (Longuet-Higgins, 1953). Similar to the wave breaking induced accelerations implemented above, this stress can be incorporated in the form of either a body force,

$$\mathbf{B}^{bf} = \frac{\varepsilon^{bf}}{\rho_0 \sigma} \mathbf{k} \cdot f^{bf}(z) \quad (A17)$$

or an equivalent bottom boundary stress

$$\tau_{bot}^{bf} = \rho_0 D \bar{\mathbf{B}}^{bf} = \frac{\varepsilon^{bf}}{\sigma} \mathbf{k} \quad (A18)$$

where $f^{bf}(z)$ is an upward decaying vertical distribution function given by

$$f^{bf}(z) = \frac{\cosh[k_{bf}(\zeta^c - z)]}{\int_{-h}^{\zeta^c} \cosh[k_{bf}(\zeta^c - z)] dz} \quad (A19)$$

with a decay length $k_{bf}^{-1} = a_{bf} \delta_w$, where a_{bf} is an empirical constant which is equal to one under monochromatic waves and has

a much larger value (e.g., $a_{bf}=3$ is used by Reniers et al. 2004b) under random waves (Klopman, 1994); δ_w is the wave bottom boundary layer thickness expressed as a function of the semi-orbital excursion length (A_{orb}^w), Nikuradse roughness (k_N) and bottom roughness length (z_b) (Fredsoe and Deigaard, 1992):

$$\delta_w = 0.09 k_N \left(\frac{A_{orb}^w}{k_N} \right)^{0.82} \quad (A20)$$

where $A_{orb}^w = \frac{|u_{orb}^w|}{\sigma}$ and $k_N = 30z_b$.

A5. Acceleration due to surface streaming

Due to the wave-viscous boundary layer at the water surface, a surface streaming similar to the concept of bottom streaming occurs. As the thickness of this surface wave-viscous boundary layer ($\sqrt{2\nu/\sigma} \approx 1$ mm) is usually too thin to be resolved, the acceleration due to surface streaming in the momentum balance is implemented only as a boundary stress in this study. It is parameterized as (Xu and Bowen, 1994):

$$\tau_{sur}^{swb} = \frac{\coth(kh)}{4} \rho_0 K_M H_s^2 \sigma k \cdot \mathbf{k} \quad (A21)$$

Although many studies have omitted this effect of surface streaming (e.g. U10), the effect can be significant especially outside the surf zone (Lentz et al., 2008).

Appendix B. Model transformation

Three new variables are defined,

$$\begin{aligned} \zeta^c &= \zeta + \hat{\zeta} \\ \phi^c &= \phi + \mathcal{K} \\ (\mathbf{V}^l, w^l) &= (\mathbf{V}^{st}, w^{st}) + (\mathbf{V}, w) \end{aligned} \quad (B1)$$

where ζ^c is the composite sea level, ϕ^c is the sum of the dynamic pressure and the Bernoulli head, and (\mathbf{V}^l, w^l) is the wave-averaged Lagrangian velocity.

Rewritten in a flux-divergence form, the momentum and continuity equations become

$$\begin{aligned} \frac{\partial \mathbf{V}}{\partial t} + \widetilde{\nabla}_\perp \cdot (\widetilde{\mathbf{V}} \mathbf{V}) + \frac{\partial}{\partial z} (w^l \mathbf{V}) + f \hat{z} \times \mathbf{V}^l + \nabla_\perp \phi^c \\ - \mathbf{F} - \frac{\partial}{\partial z} \left(K_M \frac{\partial \mathbf{V}}{\partial z} + \nu \frac{\partial \mathbf{V}}{\partial z} \right) = \mathbf{J}' + \mathbf{F}^w \end{aligned} \quad (B2)$$

$$\frac{\partial \phi^c}{\partial z} + \frac{g\rho}{\rho_0} = K \quad (B3)$$

$$\nabla_\perp \cdot \mathbf{V}^l + \frac{\partial w^l}{\partial z} = 0 \quad (B4)$$

where \mathbf{J}' is a modified VF, expressed as

$$\begin{aligned} \mathbf{J}' &= -\hat{z} \times \mathbf{V}^{st} (f + (\hat{z} \cdot \nabla_\perp \times \mathbf{V})) + \mathbf{V} \frac{\partial w^{st}}{\partial z} \\ &= -\hat{z} \times \mathbf{V}^{st} (f + (\hat{z} \cdot \nabla_\perp \times \mathbf{V})) - \mathbf{V} (\nabla_\perp \cdot \mathbf{V}^{st}) \end{aligned} \quad (B5)$$

After these steps the wave-induced terms are no longer retained to the right hand side. The boundary conditions become

$$\begin{aligned} w^l|_{-h} + \mathbf{V}|_{-h} \cdot \nabla_\perp h &= 0 \\ w^l|_{\zeta^c} - \frac{\partial \zeta^c}{\partial t} - (\mathbf{V}|_{\zeta^c} \cdot \nabla_\perp) \zeta^c &= 0 \\ g \zeta^c - \phi^c|_{\zeta^c} = \mathcal{P} + g \hat{\zeta} - \mathcal{K}|_{\zeta^c} \end{aligned} \quad (B6)$$

The depth-integrated continuity equation is given by

$$\frac{\partial \zeta^c}{\partial t} + \nabla_\perp \cdot \widetilde{\mathbf{V}}^l = 0 \quad (B7)$$

where $\bar{\mathbf{V}}^l$ is the depth integral of \mathbf{V}^l .

Subsequently, we define

$$(\mathbf{V}^l, \omega^l) = (\mathbf{V}^{st}, \omega^{st}) + (\mathbf{V}, \omega) \quad (\text{B8})$$

where ω , ω^{st}, ω^l are the vertical Eulerian, Stokes and Lagrangian velocities in Sigma coordinates, respectively. The equations for the wave-averaged currents can then be transformed into the sigma coordinates used by FVCOM:

$$\frac{\partial D}{\partial t} + \frac{\partial u^l D}{\partial x} + \frac{\partial v^l D}{\partial y} + \frac{\partial \omega^l}{\partial s} = 0 \quad (\text{B9})$$

$$\begin{aligned} \frac{\partial u D}{\partial t} + \frac{\partial u^2 D}{\partial x} + \frac{\partial uv D}{\partial y} + \frac{\partial u \omega^l}{\partial s} - f v^l D + D \frac{\partial \phi^c}{\partial x} \\ - DF_x - \frac{\partial}{\partial s} \left(\frac{K_H}{D} \frac{\partial u}{\partial s} + \frac{\nu}{D} \frac{\partial u}{\partial s} \right) = D v^{st} \left(\frac{\partial v}{\partial x} - \frac{\partial u}{\partial y} \right) \\ - u \left(\frac{\partial u^{st} D}{\partial x} + \frac{\partial v^{st} D}{\partial y} \right) + DF_x^w \end{aligned} \quad (\text{B10})$$

$$\begin{aligned} \frac{\partial v D}{\partial t} + \frac{\partial uv D}{\partial x} + \frac{\partial v^2 D}{\partial y} + \frac{\partial v \omega^l}{\partial s} + f u^l D + D \frac{\partial \phi^c}{\partial y} \\ - DF_y - \frac{\partial}{\partial s} \left(\frac{K_H}{D} \frac{\partial v}{\partial s} + \frac{\nu}{D} \frac{\partial v}{\partial s} \right) = -D u^{st} \left(\frac{\partial v}{\partial x} - \frac{\partial u}{\partial y} \right) \\ - v \left(\frac{\partial u^{st} D}{\partial x} + \frac{\partial v^{st} D}{\partial y} \right) + DF_y^w \end{aligned} \quad (\text{B11})$$

where $\mathbf{F} = (F_x, F_y)$ is the non-wave body force and parameterized horizontal momentum mixing term; $\mathbf{F}^w = (F_x^w, F_y^w)$ is the momentum flux from non-conservative wave terms described later in this section; the vertical sigma coordinates $s = \frac{z - \zeta^c}{D}$ ranges from $s = -1$ at the bottom to $s = 0$ at the free surface; the vertical Lagrangian velocity over the s surface is given by

$$\omega^l = \left[w^l - \left(\frac{\partial z}{\partial t} + \mathbf{V}^l \cdot \nabla_{\perp} z \right) \right] \Big|_s \quad (\text{B12})$$

The geopotential function, evaluated from integration of the vertical momentum equation, is given by

$$\phi^c = g(\zeta^c - \hat{\zeta}) - (\mathcal{P}|_{\zeta^c} - \mathcal{K}|_{\zeta^c}) + \int_s^0 \left[\frac{g\rho}{\rho_0} - K \right] D ds \quad (\text{B13})$$

References

Agrawal, Y.C., Terray, E.A., Donelan, M.A., Hwang, P.A., Williams, A.J., Drennan, W.M., Kahma, K.K., Kitaigorodskii, S.A., 1992. Enhanced dissipation of kinetic energy beneath surface waves. *Nature* 359, 219–220.

Aiki, H., Greatbatch, R.J., 2013. The vertical structure of the surface wave radiation stress for circulation over a sloping bottom as given by thickness-weighted-mean theory. *J. Phys. Oceanogr.* 43, 149–164.

Alves, J.H.G.M., Banner, M.L., 2003. Performance of a saturation-based dissipation-rate source term in modeling the fetch-limited evolution of wind waves. *J. Phys. Oceanogr.* 33, 1274–1298.

Ardhuin, F., Raschle, N., Belibassakis, K.A., 2008a. Explicit wave-averaged primitive equations using a generalized Lagrangian mean. *Ocean Model* 20, 35–60. doi:10.1016/j.ocemod.2007.07.001.

Ardhuin, F., Jenkins, A.D., Belibassakis, K.A., 2008b. Comments on “the three-dimensional current and surface wave equations.”. *J. Phys. Oceanogr.* 38, 1340–1350. doi:10.1175/2007JPO3670.1.

Bakhoday Paskyabi, M., Fer, I., Jenkins, A.D., 2012. Surface gravity wave effects on the upper ocean boundary layer: modification of a one-dimensional vertical mixing model. *Cont. Shelf Res.* 38, 63–78.

Battjes, J.A., Janssen, J.P.F.M., 1978. Energy loss and set-up due to breaking of random waves. In: *Proceedings of the 16th International Conference on Coastal Engineering*. ASCE, pp. 569–587.

Bennis, A.C., Ardhuin, F., Dumas, F., 2011. On the coupling of wave and three-dimensional circulation models: choice of theoretical framework, practical implementation and adiabatic tests. *Ocean Model* 40, 260–272. doi:10.1016/j.ocemod.2011.09.003.

Bertotti, L., Cavaleri, L., 1994. Accuracy of wind and wave evaluation in coastal regions. In: *Proceedings of the 24th International Conference on Coastal Engineering*. ASCE, pp. 57–67.

Booij, N., Ris, R.C., Holthuijsen, L.H., 1999. A third-generation wave model for coastal regions 1. Model description and validation. *J. Geophys. Res.* 104 (C4), 7649–7666. doi:10.1029/98jc02622.

Booij, N., Haagsma, I.J.G., Holthuijsen, L.H., Kieftenburg, A.T.M.M., Ris, R.C., van der Westhuysen, A.J., Zijlema, M., 2015. SWAN Cycle III Version 41.01A Scientific and Technical Documentation. Delft University of Technology.

Bowen, A.J., Inman, D.L., Simmons, V.P., 1968. Wave ‘set-down’ and wave setup. *J. Geophys. Res.* 73, 2569–2577.

Brown, S.A., Greaves, D.M., Magar, V., Conley, D.C., 2016. Evaluation of turbulence closure models under spilling and plunging breakers in the surf zone. *Coast. Eng.* 114, 177–193. doi:10.1016/j.coastaleng.2016.04.002.

Burchard, H., 2001. Simulating the Wave-Enhanced Layer under Breaking Surface Waves with Two-Equation Turbulence Models. *J. Phys. Oceanogr.* 31, 3133–3145.

Burchard, H., Bolding, K., Villarreal, M.R., 1999. GOTM, a general ocean turbulence model. Theory, implementation and test cases, European Commission, Report EUR 18745, 103 pp.

Chen, C., Liu, H., Beardsley, R.C., 2003. An unstructured grid, finite-volume, three-dimensional, primitive equations ocean model: application to coastal ocean and estuaries. *J. Atmos. Ocean. Technol.* 20, 159–186.

Christensen, E.D., Walstra, D., Emerat, N., 2002. Vertical variation of the flow across the surf zone. *Coast. Eng.* 45, 169–198.

Craik, A.D.D., Leibovich, S., 1976. A rational model for Langmuir circulations. *J. Fluid Mech.* 73, 401–426.

Craig, P.D., Banner, M.L., 1994. Modeling wave-enhanced turbulence in the ocean surface layer. *J. Phys. Oceanogr.* 24, 2546–2559.

Craig, P.D., 1996. Velocity profiles and surface roughness under breaking waves. *J. Geophys. Res. Ocean.* 101, 1265–1277. doi:10.1029/95JC03220.

Dietrich, J.C., Zijlema, M., Westerink, J.J., Holthuijsen, L.H., Dawson, C., Luettich, R.A., Jensen, R.E., Smith, J.M., Stelling, G.S., Stone, G.W., 2011. Modeling hurricane waves and storm surge using integrally-coupled, scalable computations. *Coast. Eng.* 58 (1), 45–65.

Durski, S.M., Glenn, S.M., Haidvogel, D., 2004. Vertical mixing schemes in the coastal ocean: comparison of the level 2.5 Mellor-Yamada scheme with an enhanced version of the K profile parameterization. *J. Geophys. Res.* 109, 1–23. doi:10.1029/2002JC001702, C01015.

Elgar, S., Guza, R.T., Raubenheimer, B., Herbers, T.H.C., Gallagher, E.L., 1997. Spectral evolution of shoaling and breaking waves on a. *J. Geophys. Res.* 102, 15,797–15,805.

Fedderson, F., Guza, R.T., Elgar, S., Herbers, T.H.C., 1998. Alongshore momentum balances in the nearshore. *J. Geophys. Res.* 103, 15667–15676. doi:10.1029/98JC01270.

Fedderson, F., Trowbridge, J.H., 2005. The effect of wave breaking on surf-zone turbulence and alongshore currents: a modeling study. *J. Phys. Oceanogr.* 35, 2187–2203. doi:10.1175/JPO2800.1.

Fedderson, F., Williams III, A.J., 2007. Direct estimation of the Reynolds stress vertical structure in the nearshore. *J. Atmos. Ocean. Technol.* 24, 102–116. doi:10.1175/JTECH1953.1.

Fedderson, F., 2012a. Observations of the surf-zone turbulent dissipation rate. *J. Phys. Oceanogr.* 42, 386–399. doi:10.1175/JPO-D-11-082.1.

Fedderson, F., 2012b. Scaling surf zone turbulence. *Geophys. Res. Lett.* 39, 1–5. doi:10.1029/2012GL052970.

Fredsoe, J., Deigaard, R., 1992. *Mechanics of coastal sediment transport*. Adv. Ser. Ocean Eng. 3, 369 pages.

Gallagher, E.L., Boyd, W., Elgar, S., Guza, R.T., Woodward, B., 1996. Performance of a sonar altimeter in the nearshore. *Mar. Geol.* 133, 241–248. doi:10.1016/0025-3227(96)00018-7.

Gallagher, E.L., Elgar, S., Guza, R.T., 1998. Observations of sand bar evolution on a natural beach. *J. Geophys. Res.* 103, 3203–3215.

Garcez Faria, A.F., Thornton, E.B., Stanton, T.P., Soares, C.V., Lippmann, T.C., 1998. Vertical profiles of longshore currents and related bed stress and bottom roughness. *J. Geophys. Res.* 103, 3217–3232.

Garcez Faria, A.F., Thornton, E.B., Lippmann, T.C., Stanton, T.P., 2000. Undertow over a barred beach. *J. Geophys. Res.* 105, 16999–17010.

Garrett, C., 1976. Generation of Langmuir circulations by surface waves – a feedback mechanism. *J. Mar. Res.* 34, 116–130.

Govender, K., Mocke, G.P., Alport, M.J., 2004. Dissipation of isotropic turbulence and length-scale measurements through the wave roller in laboratory spilling waves. *J. Geophys. Res. C Ocean.* 109, 1–8. doi:10.1029/2003JC002233.

Grue, J., Kolaas, J., 2017. Experimental particle paths and drift velocity in steep waves at finite water depth 1–10. *J. Fluid Mech.* 810, R1. doi:10.1017/jfm.2016.726.

Haas, K.A., Warner, J.C., 2009. Comparing a quasi-3D to a full 3D nearshore circulation model: shorecirc and roms. *Ocean Modell.* 26, 91–103.

Hamm, L., Mory, M., Peronnard, C., 1995. Hydrodynamic measurements around a detached breakwater in a 3d wave basin Sogreah, Ingenierie, Report No.52184 R10.

Hasselmann, K., 1971. On the mass and momentum transfer between short gravity waves and larger-scale motions. *J. Fluid Mech.* 50, 189–205. doi:10.1017/S0022112071002520.

Hasselmann, K., 1974. On the spectral dissipation of ocean waves due to white capping. *Bound. Layer Meteorol.* 6, 107–127. doi:10.1007/BF00232479.

Holthuijsen, L.H., Herman, A., Booij, N., 2003. Phase-decoupled refraction-diffraction

- for spectral wave models. *Coast. Eng.* 49, 291–305. doi:[10.1016/S0378-3839\(03\)00065-6](https://doi.org/10.1016/S0378-3839(03)00065-6).
- Huang, Z.C., Hsiao, S.C., Hwung, H.H., Chang, K.A., 2009. Turbulence and energy dissipations of surf-zone spilling breakers. *Coast. Eng.* 56, 733–746. doi:[10.1016/j.coastaleng.2009.02.003](https://doi.org/10.1016/j.coastaleng.2009.02.003).
- Huang, H., Chen, C., Cowles, G., Winant, C., Beardsley, R., Hedstrom, K., Haidvogel, D., 2008. FVCOM validation experiments: comparisons with ROMS for three idealized barotropic test problems. *J. Geophys. Res.* 113, C07042. doi:[10.1029/2007JC004557](https://doi.org/10.1029/2007JC004557).
- Klopman, G., 1994. Stokes transport. WL-Delft Hydraulics Report H840.30, Part II.
- Kumar, N., Voulgaris, G., Warner, J.C., 2011. Implementation and modification of a three-dimensional radiation stress formulation for surf zone and rip-current applications. *Coast. Eng.* 58, 1097–1117. doi:[10.1016/j.coastaleng.2011.06.009](https://doi.org/10.1016/j.coastaleng.2011.06.009).
- Kumar, N., Voulgaris, G., Warner, J.C., Olabarrieta, M., 2012. Implementation of the vortex force formalism in the coupled ocean-atmosphere-wave-sediment transport (COAWST) modeling system for inner shelf and surf zone applications. *Ocean Model.* 47, 65–95. doi:[10.1016/j.ocemod.2012.01.003](https://doi.org/10.1016/j.ocemod.2012.01.003).
- Lai, Z., Chen, C., Cowles, G., Beardsley, R.C., 2010a. A Non-Hydrostatic Version of FVCOM, Part I: Validation Experiments. *J. Geophys. Res.-Oceans* 115. doi:[10.1029/2009JC005525](https://doi.org/10.1029/2009JC005525).
- Lai, Z., Chen, C., Cowles, G., Beardsley, R.C., 2010b. A Non-Hydrostatic Version of FVCOM, Part II: Mechanistic Study of Tidally Generated Nonlinear Internal Waves in Massachusetts Bay. *J. Geophys. Res.-Oceans* doi:[10.1029/2010JC006331](https://doi.org/10.1029/2010JC006331).
- Lentz, S.J., Fewings, M., Howd, P., Fredericks, J., Hathaway, K., 2008. Observations and a model of undertow over the inner continental shelf. *J. Phys. Oceanogr.* 38, 2341–2357. doi:[10.1175/2008JP03986.1](https://doi.org/10.1175/2008JP03986.1).
- Li, M., Fernando, P.T., Pan, S., O'Connor, B.A., Chen, D., 2007. Development of a quasi-3d numerical model for sediment transport prediction in the coastal region. *J. Hydro-Environ. Res.* 1, 143–156. doi:[10.1016/j.jher.2007.09.001](https://doi.org/10.1016/j.jher.2007.09.001).
- Lin, P., Liu, P.L.-F., 1998. A numerical study of breaking waves in the surf zone. *J. Fluid Mech.* 359, 239–264. doi:[10.1017/S002211209700846X](https://doi.org/10.1017/S002211209700846X).
- Long, C.E., 1996. Index and bulk parameters for frequency-direction spectrums measured at CERC Field Research Facility, June 1994 to August 1995. US Army Corps of Engineers Waterway Experiment Station, Vicksburg, MI, USA.
- Longuet-Higgins, M.S., 1953. Mass transport in water waves. *Philos. Trans. R. Soc. Lond., Ser. A* 245, 535–581.
- Longuet-Higgins, M.S., Stewart, R.W., 1964. Radiation stresses in water waves: a physical discussion, with applications. *Deep-Sea Res.* 11, 529–562.
- McWilliams, J.C., Restrepo, J.M., Lane, E.M., 2004. An asymptotic theory for the interaction of waves and currents in coastal waters. *J. Fluid Mech.* 511, 135–178. doi:[10.1017/S0022112004009358](https://doi.org/10.1017/S0022112004009358).
- Mellor, G., 2003. The three-dimensional current and surface wave equations. *J. Phys. Oceanogr.* 33, 1978–1989.
- Mellor, G., 2005. Some consequences of the three-dimensional current and surface wave equations. *J. Phys. Oceanogr.* 35, 2291–2298. doi:[10.1175/JPO2794.1](https://doi.org/10.1175/JPO2794.1).
- Mellor, G., 2011. Wave radiation stress. *Ocean Dyn.* 61, 563–568. doi:[10.1007/s10236-010-0359-2](https://doi.org/10.1007/s10236-010-0359-2).
- Mellor, G., 2015. A combined derivation of the integrated and vertically resolved, coupled wave-current equations. *J. Phys. Oceanogr.* 45, 1453–1463. doi:[10.1175/JPO-D-14-0112.1](https://doi.org/10.1175/JPO-D-14-0112.1).
- Michaud, H., Marsaleix, P., Leredde, Y., Estournel, C., Bourrin, F., Lyard, F., Mayet, C., Ardhuin, F., 2012. Three-dimensional modelling of wave-induced current from the surf zone to the inner shelf. *Ocean Sci.* 8, 657–681. doi:[10.5194/os-8-657-2012](https://doi.org/10.5194/os-8-657-2012).
- Moghim, S., Thomson, J., Özkan-Haller, T., Umlauf, L., Zippel, S., 2016. On the modeling of wave-enhanced turbulence nearshore. *Ocean Model.* 103, 118–132. doi:[10.1016/j.ocemod.2015.11.004](https://doi.org/10.1016/j.ocemod.2015.11.004).
- Nairn, R.B., Roelvink, J.A., Southgate, H.N., 1991. Transition zone width and implications for modelling surfzone hydrodynamics. In: Edge, B.L. (Ed.), *Proceedings of the 22nd Coastal Engineering International Conference 1990*. American Society of Civil Engineers, New York, Delft, The Netherlands, pp. 68–82.
- Newberger, P.A., Allen, J.S., 2007a. Forcing a three-dimensional, hydrostatic, primitive-equation model for application in the surf zone: 1. Formulation. *J. Geophys. Res.* 112, C08018. doi:[10.1029/2006JC003472](https://doi.org/10.1029/2006JC003472).
- Newberger, P.A., Allen, J.S., 2007b. Forcing a three-dimensional, hydrostatic, primitive-equation model for application in the surf zone: 2. Application to DUCK94. *J. Geophys. Res.* 112, C08019. doi:[10.1029/2006JC003474](https://doi.org/10.1029/2006JC003474).
- Phillips, O.M., 1977. *The Dynamics of the Upper Ocean*. Cambridge University Press, Cambridge.
- Qi, J., Chen, C., Beardsley, R.C., Perrie, W., Cowles, G.W., Lai, Z., 2009. An unstructured-grid finite-volume surface wave model (FVCOM-SWAVE): implementation, validations and applications. *Ocean Modell.* 28, 153–166.
- Rakha, K.A., 1998. A quasi-3D phase-resolving hydrodynamic and sediment transport model. *Coast. Eng.* 34, 277–311. doi:[10.1016/S0378-3839\(98\)00030-1](https://doi.org/10.1016/S0378-3839(98)00030-1).
- Reniars, A.J.H.M., Roelvink, J.A., Thornton, E.B., 2004a. Morphodynamic modeling of an embayed beach under wave group forcing. *J. Geophys. Res.* 109, 1–22. doi:[10.1029/2002JC001586](https://doi.org/10.1029/2002JC001586).
- Reniars, A.J.H.M., Thornton, E.B., Stanton, T.P., Roelvink, J.A., 2004b. Vertical flow structure during Sandy Duck: observations and modeling. *Coast. Eng.* 51, 237–260. doi:[10.1016/j.coastaleng.2004.02.001](https://doi.org/10.1016/j.coastaleng.2004.02.001).
- Roland, A., Ardhuin, F., 2014. On the developments of spectral wave models: numerics and parameterizations for the coastal ocean. *Ocean Dyn.* 64, 833–846. doi:[10.1007/s10236-014-0711-z](https://doi.org/10.1007/s10236-014-0711-z).
- Salmon, J.E., Holthuijsen, L.H., Zijlema, M., van Vledder, G.P., Pietrzak, J.D., 2015. Scaling depth-induced wave-breaking in two-dimensional spectral wave models. *Ocean Model.* 87, 30–47. doi:[10.1016/j.ocemod.2014.12.011](https://doi.org/10.1016/j.ocemod.2014.12.011).
- Shao, S., 2006. Simulation of breaking wave by SPH method coupled with k- ϵ model. *J. Hydraul. Res.* 44, 338–349. doi:[10.1080/00221686.2006.9521686](https://doi.org/10.1080/00221686.2006.9521686).
- Smith, E.R., Kraus, N.C., 1991. Laboratory study of wave-breaking over fixed bars and artificial reefs. *J. Waterw. Port, Coastal, Ocean Eng.* 117, 307–325.
- Soulsby, R.L., 1995. Bed shear-stresses due to combined waves and currents. In: Stive, M.J.F. (Ed.), *Advances in Coastal Morphodynamics: An Overview of the G8-Coastal Morpho-dynamics Project, Co-Sponsored by the Commission of The European Communities Directorate General XII*, pp. 4.20–4.23.
- Stips, A., Burchard, H., Bolding, K., Prandke, H., Simon, A., Wüest, A., 2005. Measurement and simulation of viscous dissipation in the wave affected surface layer. *Deep. Res. Part II Top. Stud. Oceanogr.* 52, 1133–1155. doi:[10.1016/j.dsr2.2005.01.012](https://doi.org/10.1016/j.dsr2.2005.01.012).
- Stive, M.J.F., De Vriend, H.J., 1994. Shear stresses and mean flow in shoaling and breaking waves. *Coast. Eng. Proc.* 1, 594–608. doi:[10.9753/icce.v24](https://doi.org/10.9753/icce.v24).
- Sun, Y., Chen, C., Beardsley, R.C., Xu, Q., Qi, J., Lin, H., 2013. Impact of current-wave interaction on storm surge simulation: a case study for Hurricane Bob. *J. Geophys. Res.* 118, 2685–2701. doi:[10.1002/jgrc.20207](https://doi.org/10.1002/jgrc.20207).
- Suzuki, N., Fox-Kemper, B., 2016. Understanding Stokes forces in the wave-averaged equations. *J. Geophys. Res.* 121, 3579–3596. doi:[10.1002/2015JC011563](https://doi.org/10.1002/2015JC011563).
- Svendsen, I.A., 1984. Mass flux and undertow in a surf zone. *Coastal Eng.* 8, 347–365.
- Tajima, Y., Madsen, O.S., 2006. Modeling near-shore waves, surface rollers, and undertow velocity profiles. *J. Waterway Port Coast. Ocean Eng.* 132, 429–438.
- Terray, E.A., Donelan, M.A., Agrawal, Y.C., Drennan, W.M., Kahma, K.K., Williams III, A.J., Hwang, P.A., Kitaigorodskii, S.A., 1996. Estimates of kinetic energy dissipation under breaking waves. *J. Phys. Oceanogr.* 26, 792–807.
- Terray, E.A., Drennan, W.M., Donelan, M.A., 1999. The vertical structure of shear and dissipation in the ocean surface layer. In: Banner, M.L. (Ed.), *The Wind-Driven Air-Sea Interface. Electromagnetic and Acoustic Sensing, Wave Dynamics and Turbulent Fluxes*. School of Mathematics, University of NSW, Australia, pp. 239–245.
- Thorpe, S.A., 1984. On the determination of K_v in the near-surface ocean from acoustic measurements of bubbles. *J. Phys. Oceanogr.* 14, 855–863.
- Uchiyama, Y., McWilliams, J.C., Restrepo, J.M., 2009. Wave-current interaction in nearshore shear instability analyzed with a vortex force formalism. *J. Geophys. Res.* 114, 1–15. doi:[10.1029/2008JC005135](https://doi.org/10.1029/2008JC005135), C06021.
- Uchiyama, Y., McWilliams, J.C., Schepetkin, A.F., 2010. Wave-current interaction in an oceanic circulation model with a vortex-force formalism: application to the surf zone. *Ocean Model.* 34, 16–35. doi:[10.1016/j.ocemod.2010.04.002](https://doi.org/10.1016/j.ocemod.2010.04.002).
- Umlauf, L., Burchard, H., 2003. A generic length-scale equation for geophysical. *J. Mar. Res.* 61, 235–265.
- Umlauf, L., Burchard, H., Hutter, K., 2003. Extending the $k-\omega$ turbulence model towards oceanic applications. *Ocean Model.* 5, 195–218. doi:[10.1016/S1463-5003\(02\)00039-2](https://doi.org/10.1016/S1463-5003(02)00039-2).
- Umlauf, L., Bolding, K., Burchard, H., 2005. GOTM – Scientific Documentation. Version 3.2. Baltic Sea Research Institute, Warnemünde, Germany No. 63 of Marine Science Reports.
- Van der Westhuysen, A.J., Zijlema, M., Battjes, J.A., 2007. Nonlinear saturation based whitecapping dissipation in SWAN for deep and shallow water. *Coast. Eng.* 54, 151–170.
- Van der A, D.A., Van der Zanden, J., O'Donoghue, T., Hurther, D., Cáceres, I., McLelland, S.J., Ribberink, J.S., 2017. Large-scale laboratory study of breaking wave hydrodynamics over a fixed bar. *J. Geophys. Res. Ocean.* 122, 3287–3310. doi:[10.1002/2016JC012072](https://doi.org/10.1002/2016JC012072).
- Van der Zanden, J., van der A, D.A., Hurther, D., Cáceres, I., O'Donoghue, T., Ribberink, J.S., 2016. Near-bed hydrodynamics and turbulence below a large-scale plunging breaking wave over a mobile barred bed profile. *J. Geophys. Res. Oceans* 121, 6482–6506. doi:[10.1002/2016JC011909](https://doi.org/10.1002/2016JC011909).
- Van Rijn, L., Ribberink, J., van der Werf, J., 2013. *Coastal sediment dynamics: recent advances and future research needs*. *J. Hydraul. Res.* 51 (5), 475–493.
- Wang, J., Shen, Y., 2011. Development and validation of a three-dimensional, wave-current coupled model on unstructured meshes. *Sci. China Phys., Mech. Astron.* 54, 42–58. doi:[10.1007/s11433-010-4192-x](https://doi.org/10.1007/s11433-010-4192-x).
- Warner, J.C., Sherwood, C.R., Arango, H.G., Signell, R.P., 2005. Performance of four turbulence closure models implemented using a generic length scale method. *Ocean Model.* 8, 81–113. doi:[10.1016/j.ocemod.2003.12.003](https://doi.org/10.1016/j.ocemod.2003.12.003).
- Wu, L., Chen, C., Guo, P., Shi, M., Qi, J., Ge, J., 2011. A FVCOM-based unstructured grid wave, current, sediment transport model. I. Model description and validation. *J. Ocean Univ. China (English Edition)* 10 (1), 1–8. doi:[10.1007/s11802-011-1788-3](https://doi.org/10.1007/s11802-011-1788-3).
- Xie, Z., 2013. Two-phase flow modelling of spilling and plunging breaking waves. *Appl. Math. Model.* 37, 3698–3713. doi:[10.1016/j.apm.2012.07.057](https://doi.org/10.1016/j.apm.2012.07.057).
- Xu, Z., Bowen, A.J., 1994. Wave- and wind-driven flow in water of finite depth. *J. Phys. Oceanogr.* 24, 1850–1866.
- Zijlema, M., 2010. Computation of wind-wave spectra in coastal waters with SWAN on unstructured grids. *Coast. Eng.* 57, 267–277. doi:[10.1016/j.coastaleng.2009.10.011](https://doi.org/10.1016/j.coastaleng.2009.10.011).